

TRANSIENT ANALYSIS OF CASSON FLUID THERMO-CONVECTION FROM A VERTICAL CYLINDER EMBEDDED IN A POROUS MEDIUM: ENTROPY GENERATION AND THERMAL ENERGY TRANSFER VISUALIZATION

G. J. Reddy^{1,*}, B. Kethireddy¹, M. Kumar¹ and O. Anwar Bég²

¹*Department of Mathematics, Central University of Karnataka, Kalaburagi, India-585367*

²*Fluid Mechanics, Aeronautical and Mechanical Engineering, Department, School of Computing, Science and Engineering, University of Salford, Manchester M54WT, UK*

* *Corresponding author - Email: janardhanreddy.nitw@gmail.com*

ABSTRACT

Thermal transport in porous media has stimulated substantial interest in engineering sciences due to increasing applications in filtration systems, porous bearings, porous layer insulation, biomechanics, geomechanics etc. Motivated by such applications, in this article a numerical investigation of entropy generation effects on the heat and momentum transfer in unsteady laminar incompressible boundary layer flow of a Casson viscoplastic fluid over a uniformly heated vertical cylinder embedded in a porous medium is presented. Darcy's law is employed to simulate bulk drag effects at low Reynolds number for an isotropic, homogenous porous medium. Heat line visualization is also included. The mathematical model is derived and normalized using appropriate transformation variables. The resulting time-dependent non-linear coupled partial differential conservation equations with associated boundary conditions are solved with an efficient unconditionally stable implicit finite difference Crank Nicolson scheme. The time histories of average values of momentum and heat transport coefficients, entropy generation and Bejan number, as well as the steady-state flow variables are computed for several values of non-dimensional parameters arising in the flow equations. The results indicate that entropy generation parameter and Bejan number are both elevated with increasing values of Casson fluid parameter, Darcy number, group parameter and Grashof number. To analyze the heat transfer process in a two-dimensional domain, plotting heat lines provides an excellent approach in addition to streamlines and isotherms. The dimensionless heat function values are shown to correlate closely with the overall rate of heat transfer. Bejan's heat flow visualization implies that the heat function contours are compact in the neighbourhood of the leading edge of the boundary layer on the hot cylindrical wall. It is observed that as the Darcy number increases, the deviations of heat lines from the hot wall are reduced. Furthermore the deviations of flow variables from the hot wall for a Casson fluid are significant compared with those computed for a Newtonian fluid and this has important implications in industrial thermal materials processing operations.

KEYWORDS: *Casson fluid; Entropy generation; Vertical cylinder; Finite difference method; Heat function; Porous medium.*

NOMENCLATURE

Be	dimensionless Bejan number
\overline{C}_f	dimensionless average momentum transport coefficient
c_p	specific heat
Da	Darcy number
g	acceleration due to gravity
Gr	Grashof number
k	thermal conductivity of the fluid
k_1	permeability parameter
Ns	dimensionless entropy heat generation number
\overline{Nu}	dimensionless average heat transport coefficient
Pr	Prandtl number
r_o	radius of the cylinder
r	radial coordinate
R	dimensionless radial coordinate
t'	time
t	dimensionless time
T'	temperature
u, v	velocity components in (x, r) coordinate system
U, V	dimensionless velocity components in (X, R) coordinate system
x	axial coordinate

X dimensionless axial coordinate

Greek Letters

θ dimensionless temperature

β Casson viscoplastic fluid parameter

ε_1 dimensionless viscous dissipation parameter

μ viscosity of the fluid

α thermal diffusivity

Ω' heat function

ν kinematic viscosity

Ω dimensionless heat function

ρ density

ψ dimensionless stream function

β_T volumetric coefficient of thermal expansion

$\varepsilon_1 \Theta^{-1}$ dimensionless group parameter

Θ non-dimensional temperature difference

Subscripts

w wall conditions

l, m grid levels in (X, R) coordinate system

∞ ambient conditions

Superscript

n time level

1. INTRODUCTION

Natural convection boundary layer flows external to various bodies constitute a major area of interest in thermofluid dynamics. Geometries may include cylinders, ellipses, spheres, curved walls, wavy plates, cones etc. These feature frequently in industrial manufacturing and process engineering systems. The thermal buoyancy force associated with natural convection flows can exert a critical role in determining skin friction and heat transfer rates at the boundary. The popularity of cylindrical bodies in thermal engineering has motivated an exceptional interest in analysing the free convection boundary layer flows from cylinders. Sparrow and Gregg [1] were among the first researchers to investigate free convective fluid flow from a uniformly heated vertical cylinder with asymptotic methods. Lee *et al.* [2] extended the model in [1] to the non-isothermal case for a thin vertical cylinder. These investigations were however restricted to Newtonian viscous flows i.e. they did not consider rheological effects which characterize numerous working fluids and complex materials in for example polymer processing operations. In the past several decades non-Newtonian transport phenomena have motivated considerable interest among engineers, physicists, and mathematicians. This area presents a rich spectrum of nonlinear boundary value problems largely due to the extremely diverse range of rheological models available for simulating complex flow behavior. Popular non-Newtonian models include viscoelastic models with memory effects (e.g. differential liquids, Maxwell upper convected fluids, Oldroyd-B fluids, Walters-B fluids, Johnson-Segalman fluids), shear-thinning fluids (e.g. Ostwald-DeWaele power law, Cross model, Ellis model etc), viscoplastic models (e.g. Bingham plastic, Herschel-Bulkley, Mizrahi-Berk and Vocadlo models) and polar fluid models (Eringen micropolar, Stokes polar, Bluestein-Green dipolar etc). Rani and Reddy [3] examined the time-dependent free convection of a Stokes couple stress non-Newtonian fluid in external boundary layer flow from a cylinder with cross diffusion effects. Hirschhorn *et al.* [4] investigated the pseudoplastic hydromagnetic slip flow from a plate. A particular group of viscoplastic fluids is quite accurately simulated with the *Casson model*. These include gels, foodstuffs, certain polymers, blood under certain shear rates (due to presence of several substances like fibrinogen, protein and globulin in aqueous base plasma) [5] and also paints and inks. The Casson model fits the rheological data of many real working fluids more closely than alternative viscoplastic models (e.g. Bingham model). Casson fluids are shear thinning liquids which are assumed to have an infinite viscosity at zero rate of shear, a yield stress below which no flow occurs and zero viscosity at an infinite rate of shear [6]. The Casson fluid

model was originally introduced to represent pigment-oil suspensions in printing ink [7]. It was subsequently implemented in describing the flow curves of silicon suspensions [8] and also hemodynamics [9, 10]. Owing to the applicability of this model also in polymer sheet processing, several researchers [11-12] investigated heat transfer in Casson fluid flows from a stretching surface/sheet under different conditions. Time-dependent flow of a Casson fluid over a cone and plate under the effects of chemical reaction and radiation heat flux was studied by Mythili and Sivaraj [13]. Das *et al.* [14] considered the time-dependent magnetic Casson boundary layer flow from a plate with chemical reaction and radiation. Hydromagnetic Casson flow over a sheet was investigated analytically by Nadeem *et al.* [15]. Raju *et al.* [16] analyzed the wall blowing/suction effects on Casson fluid flow from a permeable stretching heat surface with mass transfer.

Thermodynamic optimization of engineering systems has emerged as a major area of modern investigation, largely motivated by increasing efficiency and sustainability of 21st century technologies. The laws of thermodynamics and Newton's second law of motion are the basic principles on which all the flow and heat transfer systems are designed. The first law of thermodynamics provides information about the energy of the system quantitatively. On the other hand, the second law of thermodynamics that entire processes are irretrievable and it is a useful tool to examine the entropy generation to assess the irreversibility in the system. Both heat transfer and fluid friction generate entropy and this entropy generation has to be minimized to reduce the loss of available work. Entropy generation minimization (EGM) has therefore emerged as a fundamental modern technique for designing thermal systems. Entropy production determines the irreversibility related with the natural processes such as counter flow heat exchanger for gas to gas applications [17]. EGM assists the engineer in identifying which procedure, system or installation is most effectual, and it has been deployed in many sophisticated areas including turbomachinery, porous media, electric cooling, energy systems, combustion, refrigeration and materials processing. Some recent applications of entropy generation minimization analysis are pseudo-optimization design processes for solar heat exchangers [18], minimizing lost available work during heat transfer processes [19] and multi-field flows [20]. The foremost of the energy-related applications, for example, cooling of modern electronic systems, solar energy collectors, and heat energy systems rely on entropy generation. Further studies include [21-23] in which entropy generation was conducted for several flow formations.

Several researchers studied the entropy generation concept related to the heat transfer

problem for different geometries, particularly on the cylinder. Mahian *et al.* [24] examined the entropy analysis in thermal flow of electrically-conducting fluids between two vertical cylinders with different wall conditions in the presence of a magnetic field. Also, studies on entropy generation from a stretching cylinder can be found in [25]-[27]. Bassam Abu-Hijleh *et al.* [28-30] analyzed the entropy heat generation over a horizontal cylinder. Thermodynamic analysis for fluid flows between rotating cylinders were reported in [31]-[33]. Qing *et al.* [34] investigated the entropy generation in MHD Casson nanofluid convection flow over a porous surface.

Fluid dynamics in porous media arises in widespread applications including thermal insulation systems, filtration, chemical reactor design, contaminant dispersion in soils, tissue biophysics etc. Non-Newtonian fluid flows in porous media with and without heat transfer feature in chemical engineering packed beds, gel manufacture, viscous fingering in geological transport (gas and oil flows in reservoirs), digestive transport in physiology and also tribological bearings [35-37]. A popular approach is to simulate bulk porous matrix drag effects with the classical Darcy law which is valid for viscous dominated flows (low Reynolds numbers) wherein inertial effects are negated. Many authors have reported in simulations of non-Newtonian fluid flows through porous media [38-43]. Casson viscoplastic transport in porous media has also stimulated osme attention. Asma Khalid *et al.* [44] studied the transient MHD flow of Casson fluid through a porous medium over a vertical plate. Ramachandra Prasad *et al.* [45] studied the heat transfer characteristics in thermal convection of Casson fluids through non-Darcy porous media engulfing a horizontal cylinder. Transient flow of MHD Casson fluid with chemical reaction effects was analysed by Kataria and Patel [46]. Further studies include [47-48].

Thusfar relatively scant attention has been directed towards mathematical modelling of *Casson fluid flow and heat transfer from a vertical cylinder in porous media with entropy heat generation*. The present work is therefore focused on applying second law thermodynamic analysis to thermal convection in Casson viscoplastic boundary layer flow from over a uniformly heated vertical cylinder embedded in a Darcian porous media. Wall temperature is prescribed as greater than that of the surrounding fluid temperature. Entropy heat generation and momentum and heat transport coefficients are analyzed for the effects of various thermo-physical control parameters using a computational finite difference method. Solutions derived are compared with the Newtonian fluid case. The results obtained by the implicit finite difference method are corroborated with the available results in the literature.

Conventionally thermal convection fluid dynamics problems are analyzed only with the aid of streamlines and isotherms. In a given domain isotherms will furnish information on the temperature distribution. However using them to visualize the direction and heat transfer intensity is not feasible. In convection flows the direction of heat flux is not normal to the temperature contours. In these scenarios, the heat lines provide a practical methodology for visualizing the intensity of heat transfer and this in turn clarifies to the engineer possible channels for thermal energy transfer to occur from hot to cold walls. Kimura and Bejan [49] and Bejan [50] initiated the *heat line concept of flow visualization*. For cylindrical enclosures, Aggarwal and Manhapra [51] employed heatlines for the unsteady natural convective heat transfer process. Rani and Reddy [52] studied the heat lines for couple stress flows from a vertical slender cylinder. Rani *et al.* [53] studied the solutal version of this regime and presented detailed mass line visualizations. Using the same idea, recently Das and Basak [54] analyzed the rate of heat transfer at different zones within enclosures involving discrete heaters. The deployment of the heat lines approach for convection problems is further elucidated in [55]. Thusfar the heat line visualization approach has not been employed widely in heat transfer simulations for non-Newtonian fluids. The current work presents for the first time accurate and detailed visualization of Casson viscoplastic heat transfer from a cylinder with entropy generation using this heat function concept.

The organization of this research article is as follows: Section 2 presents the mathematical transport model and its non-dimensionalization for a Casson fluid flow from a semi-infinite vertical cylinder with uniform surface temperature embedded in a porous medium. Section 3 presents Crank-Nicolson numerical finite difference solutions and grid generation aspects. Section 4 includes extensive computational results (via graphs) for the transient two-dimensional flow-field profiles, average wall and heat transfer rates, entropy heat generation and Bejan number. This section also includes the heat function derivation and normalization based on the overall heat transport coefficient at the hot wall. Extensive discussion is also presented. Furthermore a comparison between Casson and Newtonian fluids is given. Finally, in section 5 key findings are summarized and possible extensions to the investigation are described.

2. MATHEMATICAL MODELLING

Transient two-dimensional laminar buoyancy-driven boundary layer flow of a Casson viscoplastic fluid over a cylinder of radius r_0 , embedded in a porous medium, is considered, as

depicted in **Fig. 1**. A rectangular coordinate system is chosen, in which the axial coordinate (x -axis) is selected from the foremost verge of the cylinder, while the radial coordinate (r -axis) is directed normal to the x -axis. The neighboring fluid temperature is considered to be stationary and similar to that of free stream temperature T'_∞ . At the outset, i.e. $t' = 0$, the temperature T'_∞ is uniform for the cylinder and surrounding fluid. Later ($t' > 0$), the temperature of the vertical cylinder is augmented to $T'_w (> T'_\infty)$ and preserved uniformly thereafter. The influence of viscous dissipation is presumed to be insignificant in the thermal equation.

The rheological equation of state for a viscous incompressible Casson fluid is given by [7]:

$$\tau_{ij} = \begin{cases} 2(\mu_B + p_y/\sqrt{2\pi})e_{ij}, & \pi > \pi_c \\ 2(\mu_B + p_y/\sqrt{2\pi_c})e_{ij}, & \pi < \pi_c \end{cases} \quad (1)$$

Here, τ_{ij} and e_{ij} represent the $(i, j)^{\text{th}}$ component of the shear stress tensor and deformation rate respectively, p_y is the yield stress of the fluid and $\pi = e_{ij}e_{ij}$, where π denotes product of the component of deformation rate with itself, π_c denotes a critical value of this product based on the non-Newtonian model and μ_B is plastic dynamic viscosity of the non-Newtonian fluid. If shear stress is less than the yield stress applied to the fluid, the fluid acts like a solid, whereas if shear stress exceeds the yield stress, motion is initiated. Implementing the Boussinesq approximation (linear variation in density) the appropriate conservation equations for mass, momentum and heat transfer for thermal free convection boundary layer flow of a Casson fluid in a Darcian porous medium assume the form [47-48]:

$$\frac{\partial(ru)}{\partial x} + \frac{\partial(rv)}{\partial r} = 0 \quad (2)$$

$$\frac{\partial u}{\partial t'} + u \frac{\partial u}{\partial x} + v \frac{\partial u}{\partial r} = \nu \left(1 + \frac{1}{\beta}\right) \left(\frac{\partial^2 u}{\partial r^2} + \frac{1}{r} \frac{\partial u}{\partial r}\right) + g\beta_T(T' - T'_\infty) - \frac{\nu}{k_1} u \quad (3)$$

$$\frac{\partial T'}{\partial t'} + u \frac{\partial T'}{\partial x} + v \frac{\partial T'}{\partial r} = \frac{\alpha}{r} \frac{\partial}{\partial r} \left(r \frac{\partial T'}{\partial r}\right) \quad (4)$$

The associated initial and boundary conditions are given by:

$$t' \leq 0: T' = T'_\infty, u = 0, v = 0, \quad \forall x \text{ and } r$$

$$t' > 0: T' = T'_w, u = 0, v = 0 \quad \text{at } r = r_0$$

$$T' = T'_\infty, u = 0, v = 0 \quad \text{at } x = 0 \quad (5)$$

$$T' \rightarrow T'_\infty, u \rightarrow 0, v \rightarrow 0 \quad \text{as } r \rightarrow \infty$$

where $\beta = \mu_B \sqrt{2\pi_c/p_y}$ is the Casson viscoplastic parameter.

Introducing the following non-dimensional quantities:

$$U = Gr^{-1} \frac{ur_0}{v}, \quad V = \frac{vr_0}{v}, \quad t = \frac{vt'}{r_0^2}, \quad X = Gr^{-1} \frac{x}{r_0}, \quad Pr = \frac{v}{\alpha}, \quad \theta = \frac{T' - T'_\infty}{T'_w - T'_\infty}, \quad Gr = \frac{g\beta r_0^3 (T'_w - T'_\infty)}{v^2},$$

$$R = \frac{r}{r_0}, \quad \Theta = \frac{T'_w - T'_\infty}{T'_\infty}, \quad \varepsilon_1 = \frac{\mu v^2}{k(T'_w - T'_\infty)r_0^2}, \quad Da = \frac{k_1}{r_0^2}, \quad \nu = \frac{\mu}{\rho} \quad (6)$$

(for the above symbols refer to the nomenclature) in Eqns. (2)- (4) and also in Eqn. (5), the unsteady boundary layer equations reduce to the following form:

$$\frac{\partial U}{\partial X} + \frac{\partial V}{\partial R} + \frac{V}{R} = 0 \quad (7)$$

$$\frac{\partial U}{\partial t} + U \frac{\partial U}{\partial X} + V \frac{\partial U}{\partial R} = \theta + \left(1 + \frac{1}{\beta}\right) \left(\frac{\partial^2 U}{\partial R^2} + \frac{1}{R} \frac{\partial U}{\partial R}\right) - \frac{1}{Da} U \quad (8)$$

$$\frac{\partial \theta}{\partial t} + U \frac{\partial \theta}{\partial X} + V \frac{\partial \theta}{\partial R} = \frac{1}{Pr} \left(\frac{\partial^2 \theta}{\partial R^2} + \frac{1}{R} \frac{\partial \theta}{\partial R}\right) \quad (9)$$

$$t \leq 0: \theta = 0, U = 0, V = 0, \quad \forall X \text{ and } R$$

$$t > 0: \theta = 1, U = 0, V = 0 \quad \text{at } R = 1$$

$$\theta = 0, U = 0, V = 0 \quad \text{at } X = 0$$

$$\theta \rightarrow 0, U \rightarrow 0, V \rightarrow 0 \quad \text{as } R \rightarrow \infty \quad (10)$$

3. FINITE DIFFERENCE NUMERICAL SOLUTIONS

Analytical solutions of the time-dependent Eqns. (7) - (9) are intractable. A computational approach is therefore selected based on the unconditionally stable finite difference iteration scheme known as the Crank-Nicolson method. The finite difference discretized versions of Eqns. (7)-(9) take the form:

$$\frac{U_{l,m}^{n+1} - U_{l-1,m}^{n+1} + U_{l,m}^n - U_{l-1,m}^n}{2\Delta X} + \frac{V_{l,m}^{n+1} - V_{l,m-1}^{n+1} + V_{l,m}^n - V_{l,m-1}^n}{2\Delta R} + (JR)V_{l,m}^{n+1} = 0 \quad (11)$$

$$\begin{aligned}
& \frac{U_{l,m}^{n+1} - U_{l,m}^n}{\Delta t} + \frac{U_{l,m}^n}{2\Delta X} (U_{l,m}^{n+1} - U_{l-1,m}^{n+1} + U_{l,m}^n - U_{l-1,m}^n) + \frac{V_{l,m}^n}{4\Delta R} (U_{l,m}^{n+1} - U_{l,m-1}^{n+1} + U_{l,m}^n - U_{l,m-1}^n) \\
&= \frac{\theta_{l,m}^{n+1} + \theta_{l,m}^n}{2} + JR \left(1 + \frac{1}{\beta}\right) \left(\frac{U_{l,m+1}^{n+1} - U_{l,m-1}^{n+1} + U_{l,m+1}^n - U_{l,m-1}^n}{4(\Delta R)}\right) + \\
&\quad \left(1 + \frac{1}{\beta}\right) \left(\frac{U_{l,m+1}^{n+1} - 2U_{l,m}^{n+1} + U_{l,m-1}^{n+1} + U_{l,m+1}^n - 2U_{l,m}^n + U_{l,m-1}^n}{2(\Delta R)^2}\right) - \frac{1}{Da} \frac{(U_{l,m}^{n+1} + U_{l,m}^n)}{2} \quad (12)
\end{aligned}$$

$$\begin{aligned}
& \frac{\theta_{l,m}^{n+1} - \theta_{l,m}^n}{\Delta t} + \frac{U_{l,m}^n}{2\Delta X} (\theta_{l,m}^{n+1} - \theta_{l-1,m}^{n+1} + \theta_{l,m}^n - \theta_{l-1,m}^n) + \frac{V_{l,m}^n}{4\Delta R} (\theta_{l,m}^{n+1} - \theta_{l,m-1}^{n+1} + \theta_{l,m}^n - \theta_{l,m-1}^n) \\
&= \left[\frac{\theta_{l,m+1}^{n+1} - 2\theta_{l,m}^{n+1} + \theta_{l,m-1}^{n+1} + \theta_{l,m+1}^n - 2\theta_{l,m}^n + \theta_{l,m-1}^n}{2Pr(\Delta R)^2}\right] + (JR) \left[\frac{\theta_{l,m+1}^{n+1} - \theta_{l,m-1}^{n+1} + \theta_{l,m+1}^n - \theta_{l,m-1}^n}{4Pr(\Delta R)}\right] \quad (13)
\end{aligned}$$

$$\text{where } JR = \frac{1}{[1+(m-1)\Delta R]}.$$

The finite difference equations are solved on a rectangular grid with $X_{max} = 1$, $X_{min} = 0$, $R_{max} = 20$ and $R_{min} = 1$ where R_{max} relates to $R = \infty$ which lies far away from the thermal and hydrodynamic (momentum) boundary layers.

3.1 Grid Independence Study

To attain an economical and consistent grid scheme for the simulations, a grid independency test has been conducted using four different grid sizes of 25 X 125, 50 X 250, 100 X 500 and 200 X 1000. The values of the average skin-friction coefficient (\overline{C}_f) and Nusselt number (\overline{Nu}) on the boundary $R = 1$ are shown in **Table 1**. A regular grid is used for all cases. It is observed from Table 1 that the 100 X 500 grid compared with 50 X 250 and 200 X 1000 grids does not tangibly modify the results for \overline{C}_f and \overline{Nu} . Hence according to this observation, a uniform grid size of 100 X 500 is of adequate accuracy for the current problem with the mesh stepping distances of 0.01 and 0.03 in axial and radial directions, respectively. Similarly to produce a reliable result with respect to time, a grid independent test has been performed for different time step sizes and is summarized in **Table 2**. The effective time step size Δt ($t = n\Delta t, n = 0, 1, 2, \dots$) is fixed as 0.01.

The finite difference procedure begins by computing the solution to the heat conservation (thermal boundary layer) Eqn. (9), which gives the temperature field. Following this the momentum transport and mass conservation Eqns. (8) and (7) are solved to yield the velocity solution. Eqns. (12) - (13) at the $(n+1)^{\text{th}}$ stage using the known n^{th} stage values are specified in the following tridiagonal form:

$$a_{l,m}\Phi_{l,m-1}^{n+1} + b_{l,m}\Phi_{l,m}^{n+1} + c_{l,m}\Phi_{l,m+1}^{n+1} = d_{l,m}^n \quad (14)$$

where Φ signifies the time-dependent flow field variables θ and U . Thus, Eqns. (12) - (13) at each interior grid point on a precise l -level comprise a system of tridiagonal equations. For a more detailed description of this finite difference scheme the reader is referred to Rani *et al.* [56].

4. RESULTS AND DISCUSSION

To study the unsteady behavior of the primary variables, such as temperature and velocity, their values are illustrated at one location neighboring the hot cylindrical wall. The time-independent state temperature and velocity profiles are presented along the radial coordinate at $X=1.0$. The computed variables for the case of Newtonian fluids in the absence of a porous medium ($\beta = \infty$) are similar with those of Lee *et al.* [2] for Prandtl number (Pr) = 0.7 and are illustrated in **Fig. 2**. Generally close correlation is achieved which confirm the validity and accuracy of the current numerical scheme. The simulated results are represented to describe the variation of the dimensionless flow variables, stream & heat functions, entropy generation number (Ns) and Bejan number (Be) which are examined along with average skin-friction and heat transport coefficients for different thermophysical control parameters. Such variations are plotted in the following subsections.

4.1 Flow Variables

Velocity:

Fig. 3 displays the transient non-dimensional velocity (U) against time (t) at the location (1, 2.02) for different values of Casson fluid parameter (β) and Darcy number (Da). Figure 3a shows the unsteady velocity profile for different values of β with $Da = 5$ and Fig. 3b for the variation of Da with $\beta = 1$. From Figs. 3a and 3b it is observed that the velocity is enhanced with time (i.e. boundary layer flow acceleration), attains the temporal peak, then marginally decreases

and finally leads to the time-independent state. For instance, in Fig. 3a when $\beta = 1.0$ and $Da = 5$, with time the wall velocity monotonically escalates, reaches temporal maxima and at last attains the asymptotic steady-state. Also, it is perceived that when $t \ll 1$, the conduction dominates the heat transfer. Subsequently, there occurs a time stage where the heat transfer rate is influenced by the effect of natural convection and this accelerates the Casson fluid flow with respect to time. Later before attaining the steady-state, the velocities are found to overshoot. Fig. 3a also shows that initially transient velocity profiles concur with each other for $t < 0.4$ whereas subsequently they diverge for $t \geq 0.4$. Furthermore the overshoot of the U profile is elevated as β is increased. The incentive behind this increment is that increasing β values decreases the size of the viscous shear diffusion terms in Eq. (7) which manifests in a reduction in resistance to the fluid flow in the province of the temporal peak of velocity. For all values of Da with fixed $\beta = 1$, Fig. 3b shows that it has the similar transient characteristics as the deviation of velocity profile pertaining to β as shown in Fig. 3a. As illustrated in Fig. 3a it is observed that initially transient velocity profiles merge with each other for $t < 1$ and then diverge for $t \geq 1$. Also, the overshoot of the U profile increases as Da is enhanced, since greater Darcy number corresponds to higher permeability of the porous medium and an associated depletion in bulk matrix drag of the porous medium fibers. The flow is therefore accelerated with higher Darcy number. From Figs. 3a and 3b it is evident that the time to attain the *temporal maxima* decreases for the velocity when β or Da increase. Also, from Fig. 3a it is observed that the time to attain the *steady-state* increases when β increases and the converse response is computed for increasing Da in Fig. 3b. These observations are confirmed in **Table 3**. Also, with the aid of Fig. 4, these velocity fluctuations pertaining to β and Da are analyzed next. Along the radial direction at $X = 1.0$ the time-independent state velocity (U) versus R is plotted in Fig. 4 for various values of β and Da . Fig. 4a shows the unsteady velocity profile for different values of β with $Da = 5$ and Fig. 4b for the effect of Da with $\beta = 1$ (note that the Newtonian case is retrieved only for infinite β values). Clearly the U curves begin with zero value at the cylinder surface, attain the peak value and thereafter monotonically shrink to zero in the direction of R . It is also noticed that in the neighborhood of surface of the cylinder the magnitude of U along the axis of the cylinder quickly rises as the value of R is increased from R_{min} ($=1$). From the Fig. 4a it is noted that near to the hot wall of the cylinder (i.e. in the region $1 < R < 4.5$) the velocity increases as β increases and the opposite pattern is observed in the region for $R \geq 4.5$ i.e., in the zone which is away from the hot wall, the peak value of velocity moves towards

with augmented velocity boundary layer thickness. This is due to the fact that augmenting the values of β leads to the decrease of the total viscosity of the Casson fluid thus increasing the peak fluid velocity. From the Fig. 4b it is noted that near to the hot wall of the cylinder the velocity increases as Da increases. Since Da increases the permeability of the medium is also elevated which as elaborated earlier reduces the bulk impedance of the solid fibers (note that the purely fluid case is retrieved for infinite permeability which implies a vanishing Darcian drag force in the momentum equation). Also Figs. 4a and 4b show that the U profiles attain their peak value nearly at (1, 2.4). From the above results, it can be noticed that there is a significant difference between the transient velocity profiles of the Casson fluid and the Newtonian fluid ($\beta = \infty$).

Temperature:

Simulated transient temperature (θ) profiles are illustrated at the spatial coordinates (1, 1.53) against time in **Fig. 5**. Figure 5a shows the effect of β with $Da = 5$ and Fig. 5b for the effect of Da with $\beta = 1$. These profiles initially oscillate with time, and after reaching a maximum value, they become independent of time. This transient behavior of the temperature is observed at other locations also. During the early period, the periodic nature of the time-dependent temperature profiles is mainly noticeable. From Fig. 5a it is noticed that for different values of β , the time-dependent temperature profiles firstly overlap with each other and then differ after a particular time. It is further observed that the peak temperature value decreases as the Casson fluid parameter increases implying that greater viscoplastic effect serves to cool the regime and to decrease thermal boundary layer thickness. Figure 5b illustrates that for all values of Da with $\beta = 1$ the same transient features are computed in temperature distributions as encountered earlier in Fig 5a with Da fixed and β varied. Also, it is observed that as the Da rises the temperature decreases. The decrease in presence of solid fibers in the porous medium with higher permeability (i.e. larger Da) results in a diminished *thermal conduction* effect. This cools the regime and lowers temperatures also decreasing thermal boundary layer thickness. From Figs. 5a and 5b it is also noted that the time needed to attain the temporal peak decreases as Da or β increases.

The simulated time-independent state θ curves for various values of β and Da against the R are shown in **Fig. 6**. Figure 6a reveals the effect of Casson fluid parameter (β) with $Da = 5$ and

Fig. 6b for Da with $\beta = 1$. These figures indicate that the temperature (θ) curves commence with a hot wall temperature and then decay progressively to the free stream zero value along the axis R . In Fig. 6a it is also noticed that the time-independent state temperature (θ) profile decreases with Casson viscoplastic effect i.e. with greater β values. Larger β gives rise to thicker temperature profiles since a larger β induces deceleration in the flow which aids thermal diffusion. Also, the time taken to reach the *time-independent state* rises as β rises. Figure 6b reveals that the time-independent temperature value is diminished with greater Da . Also, time taken to achieve the time-independent state decreases as Da increases.

4.2 Friction and Heat Transport Coefficients

The momentum and heat transport coefficients are important parameters in heat transfer studies due to their direct involvement in the convection process. The non-dimensional average momentum and heat transport coefficients are given by $\overline{C}_f = \left(1 + \frac{1}{\beta}\right) \int_0^1 \left(\frac{\partial U}{\partial R}\right)_{R=1} dX$ and $\overline{Nu} = - \int_0^1 \left(\frac{\partial \theta}{\partial R}\right)_{R=1} dX$, respectively. The values of \overline{C}_f for different β and Da are shown in Fig. 7. In Figs. 7a and 7b, it is noticed that initially for all values of β and Da , skin friction \overline{C}_f rises with t , reaches the peak value, then slightly dwindles, finally attaining the asymptotically time-independent state. This is true since the buoyancy-induced flow-field velocity is comparatively small during the initial time-dependent period, as indicated in Fig. 3, and the average momentum transport coefficient remains small, as observed in Fig. 7. It is also witnessed from Fig. 7a that, \overline{C}_f decreases for escalating values of β and the reverse trend is seen for Da in Fig. 7b. It is apparent from Figs. 7a and 7b, that in the starting time, the influence of the Casson viscoplastic parameter (β) on \overline{C}_f is more prominent than the Darcy parameter (Da). This observation is true since the amplified value of Casson fluid parameter (β) causes an increase in the fluid viscosity which in turn retards the flow i.e. decreases the U values in the boundary layer zone. Additionally Fig. 7 demonstrates that skin friction, \overline{C}_f for the Casson fluid is greater than that of the Newtonian fluid.

The average heat transport coefficient (\overline{Nu}) for several values of β and Da is graphically shown in Figs. 8a and 8b, respectively. In these figures it can be noted that, for all values of β and Da , in the beginning time the \overline{Nu} drastically decreases, then slightly increases and finally achieves the time-independent state. Also, for each value of β and Da it is evident that in the starting time

the \overline{Nu} curves overlaps with each other and thereafter deviate once some time has elapsed. This shows that in the early intervals of time heat conduction is the dominant heat transfer mode whereas with further time elapsing thermal conduction is subjugated by the thermal convection mode. Figures 8a and 8b demonstrates that an upsurge in β or Da leads to increasing values of the \overline{Nu} . It is apparent that escalating β values increase the spatial decay of the temperature flow-field in the vicinity of the hot wall owing to flow deceleration close to the surface, causing an increase in heat transfer rate to the wall i.e. \overline{Nu} . Additionally the heat transport coefficient is influenced by the temperature gradient. In Fig. 8b, it is seen that in the early intervals of time, i.e. $t \in (0, 1.9)$, \overline{Nu} is almost the same for increasing values of Da (i.e. with higher k_1) i.e. a variation in permeability does not markedly modify heat transfer rates at the wall. However with further passage of time, \overline{Nu} is significantly enhanced with increasing values of Da and reaches the *time-independent* state. A further pertinent point of interest is that in Fig. 8 \overline{Nu} for a Casson fluid is substantially lower than that of the Newtonian fluid.

4.3. Entropy heat generation analysis and Bejan number

The entropy generation per unit volume for Casson fluid with constant density is given as:

$$S_{gen} = \frac{k}{T_{\infty}'^2} \left(\frac{\partial T'}{\partial r} \right)^2 + \frac{\mu}{T_{\infty}'} \left(1 + \frac{1}{\beta} \right) \left(\frac{\partial u}{\partial r} \right)^2 + \frac{\mu}{k_1 T_{\infty}'} u^2 \quad (15)$$

The equation (15) can be rewritten as:

$$S_{gen} = S_1 + S_2 + S_3 \quad (16)$$

The individual terms are defined by:

$$S_1 = \frac{k}{T_{\infty}'^2} \left(\frac{\partial T'}{\partial r} \right)^2, S_2 = \frac{\mu}{T_{\infty}'} \left(1 + \frac{1}{\beta} \right) \left(\frac{\partial u}{\partial r} \right)^2, S_3 = \frac{\mu}{k_1 T_{\infty}'} u^2 \quad (17)$$

Here S_1 signifies the entropy generation produced by *heat flow*, S_2 denotes the entropy generation due to *viscous dissipation* for a constant density Casson fluid, S_3 denotes the entropy generation due to *porous medium effects*.

The non-dimensional entropy heat generation parameter Ns is defined as the ratio of the *volumetric entropy heat generation rate* to the *characteristic entropy heat generation rate*. Accordingly, the entropy heat generation parameter is written as [57]:

$$Ns = \left(\frac{\partial\theta}{\partial R}\right)^2 + \frac{\varepsilon_1(Gr)^2}{\Theta} \left(1 + \frac{1}{\beta}\right) \left(\frac{\partial U}{\partial R}\right)^2 + \frac{\varepsilon_1(Gr)^2}{Da} U^2 \quad (18)$$

where $\Theta = \frac{(T'_w - T'_\infty)}{T'_\infty}$ is the non-dimensional temperature difference, and the characteristic entropy heat generation is $\frac{k(T'_w - T'_\infty)^2}{T'_\infty{}^2 r_0^2}$. The equation (14) can be rewritten in the following form

$$Ns = N_1 + N_2 \quad (19)$$

where $N_1 = \left(\frac{\partial\theta}{\partial R}\right)^2$ and $N_2 = \frac{\varepsilon_1(Gr)^2}{\Theta} \left\{ \left(1 + \frac{1}{\beta}\right) \left(\frac{\partial U}{\partial R}\right)^2 + \frac{\varepsilon_1(Gr)^2}{Da} U^2 \right\}$ designate the irreversibility owing to *heat transfer* and *fluid friction (viscous dissipation)*, respectively.

To assess the *irreversibility distribution*, the parameter *Be* (Bejan number) is defined as the ratio of *entropy heat generation due to heat transfer* to the *overall entropy heat production*, and is given by

$$Be = \frac{N_1}{N_1 + N_2} \quad (20)$$

From the Eq. (20), it is understood that the Bejan number lies between 0 to 1 i.e. $0 \leq Be \leq 1$. Consequently, $Be = 0$ reveals that the parameter N_2 dominates the parameter N_1 , whereas $Be = 1$ indicates that the parameter N_1 dominates the parameter N_2 . It is evident that at $Be = 0.5$, the contribution of fluid friction in the entropy generation production is equal to irreversibility due to heat transfer i.e. $N_2 = N_1$.

The influence of the different flow-field parameters upon entropy generation (Ns) versus time (t) at the location (1, 2.40) is presented in Fig. 9. The impact of Casson fluid parameter (β), Darcy parameter (Da), Grashof number (Gr) and group parameter ($\varepsilon_1 \theta^{-1}$) on transient Ns profiles are depicted in **Figs. 9a - 9d**, respectively. From these plots, it is ascertained that, initially, the Ns curves increase radically, then decrease, then again ascend, reach a temporal peak, and finally become independent of time. This transient behavior of Ns is observed at other locations also. During the early period, the time-dependent nature of the entropy profiles is more dramatic. From Fig. 9a it is noticed that for different values of β , the time-dependent entropy profiles firstly overlap with each other and then differ after a particular time. This indicates that at initial time levels (i.e., $t < 1.2$) thermal conduction is more dominated than the convection heat transfer. After some time,

there occurs a stage when the rate of heat transfer is swayed by the influence of free convection with rising entropy production with time. As this transient period is nearing completion and just before reaching the *time-independent* state, there occur overshoots in the entropy profile. From Fig.9a, it is noted that the Ns increase with increasing β . In Fig. 9b it may be deduced that as Da increases the transient entropy heat generation number reduces strongly and becomes weak in the interval $t \in [1.6, 6.1]$ and the reverse trend is observed for $t > 6.1$. From Figs. 9a and 9b, it is understood that the time to achieve temporal peak decreases as β or Da increases. In Figs. 9c and 9d, it is evident that, initially, the Ns curves increase radically, then decrease, next upsurge, reach a temporal peak, and finally attain the time-independent state. The important observation noted here is that in the initial time phase all the Ns curves converge with each other and only deviate after some time for all values of the control parameters. The time taken to attain the temporal peak slightly decreases as Gr or $\varepsilon_1\Theta^{-1}$ increases. Thus an elevation in values of Grashof number (i.e. stronger thermal buoyancy force relative to viscous hydrodynamic force) results in increased entropy production.

The simulated time-independent dimensionless Ns profile for different hydrodynamic and thermal control parameters β , Da , Gr and $\varepsilon_1\Theta^{-1}$ along the radial direction at $X = 1.0$ are presented in Figs. 10a - 10d, respectively. As the radial position increases, the Ns magnitudes substantially increase quickly arriving at the peak value. Following this there is a sharp descent and then a gradual monotonic decay to zero. Ns values are sharpened at the peak value in the neighborhood of the hot cylindrical wall. However, the velocity curves are smoother at the peak value as shown in Figs. 4a and 4b. The entropy production results in a thinner boundary layer for all values of control parameters, which is attributable to higher entropy production adjacent to the hot wall. Figure 10a represents the effect of β on Ns . As viscoplastic Casson parameter, β , is increased, there is a strong enhancement in steady-state Ns values in close proximity to the cylinder wall (i.e., in the interval $R \in [1, 3.5]$), and subsequently there is a depression in Ns magnitudes when $R > 3.5$. The increase in the heat transport coefficient near to the cylinder surface results in an elevation in entropy generation, Ns (Fig. 8a). From Fig. 10b, with increasing value of Da the entropy profiles are boosted near to the cylinder wall (i.e., in the interval $R \in [1, 3]$), however they are subsequently decreased when $R > 3$. It is observed that as either Da or β are increased the entropy curves initially merge with each other but later diverge with greater values of radial coordinate, R .

Therefore the variation of Da on Ns is of a similar nature to the impact computed with increasing Casson viscoplastic parameter, β . Fig. 10a further indicates that the entropy production near to the hot wall (i.e. in the interval $1 < R < 3.51$) for a Casson fluid is of lower magnitude in comparison with that of a Newtonian fluid ($\beta = \infty$) and the opposite tendency is computed in the interval $R \geq 3.51$. From the Figs. 10a and 10b, it is identified that the time taken to achieve the *steady-state* is elevated with increasing values of β , whereas with increasing values of Darcy number, Da , this trend is reversed. In other words lower viscosity of the non-Newtonian liquid and higher permeability of the porous medium respectively delay and quicken the time to achieve steady-state entropy production. Figures 10c and 10d reveal that, in the neighborhood of a hot cylindrical wall, the entropy increases rapidly, then decrease drastically, and approach to zero along the radial coordinate. It is also noted that with greater values of Gr or $\varepsilon_1 \Theta^{-1}$, the Ns magnitudes are enhanced, which is induced by higher fluid friction at larger values of Grashof number or group parameter. Furthermore Figs. 10c and 10d indicate that the time needed to attain steady-state conditions is suppressed slightly with increasing values of $\varepsilon_1 \Theta^{-1}$ or Gr .

The evolution of Bejan number (Be) with time (t) at the point (1, 2.40) is plotted in Figs. 11a - 11d for selected ranges of the parameters β , Da , Gr and $\varepsilon_1 \Theta^{-1}$, respectively. These figures imply that initially Be commences with zero value, increases drastically and attains the peak value, then drops marginally, and finally becomes independent of time after a slight fluctuation. In the initial stages of flow the irreversibility due to *heat transfer* controls the entropy and when $t > 0.45$ the *fluid friction* dominates. Fig. 11a generally demonstrates that as β is increased, there is a significant reduction in Bejan number in the interval $t \in [0, 0.4]$; however this behaviour is reversed for $t > 0.4$. From Fig. 11b it is evident that increasing Da manifests in decreasing values in Be . Another important observation in Figs. 11a and 11b is that the time taken to reach the temporal peak decreases as β or Da increase. Figs. 11c and 11d reveal that, as Gr or $\varepsilon_1 \Theta^{-1}$ rises, there is a resultant elevation in Bejan number and additionally it is emphasized that the time elapse before a temporal peak and the time-independent state are attained follows a similar behaviour to that computed as Gr or $\varepsilon_1 \Theta^{-1}$ are increased.

Finally, **Figs. 12a-d** illustrate the distribution of time-independent state Bejan number, Be versus radial coordinate at $X = 1.0$ for variation in β , Da , Gr and $\varepsilon_1 \Theta^{-1}$, respectively. Invariably the steady-state characteristics of Bejan number are similar to the time-independent state entropy

generation (N_s) described earlier in Figs. 10a - 10d. From Fig. 12a as β rises it is seen that the steady-state Be increases in the interval $R \in (1, 1.3)$, then decreases in the interval $R \in (1.3, 2.15)$ and again increases in the interval $R \in (2.15, 4.6)$. Similarly in Fig. 12b the same trend is obtained for rising values of Da . Figs. 12c and 12d reveal that, in the neighborhood of the hot cylindrical wall, the Bejan number increases rapidly, then decrease drastically, and eventually approaches a vanishing value at high values of the radial coordinate. With increasing values of Gr or $\varepsilon_1\Theta^{-1}$, Bejan numbers are clearly enhanced. A noteworthy feature of both Figs 10 and 12 is that the steady-state entropy production *exceeds* the Bejan number near the wall. This confirms that smaller Be yields an increase in N_2 , i.e., $N_1 < N_2$ (refer to Eqn. 19) and thus *irreversibility due to heat transfer is dominated by fluid friction* which results in enhanced entropy production in the neighborhood of the hot wall. Figs. 12c and 12d further indicate that the time needed to attain steady-state is almost the same with increasing values of $\varepsilon_1\Theta^{-1}$ or Gr . Fig. 12b additionally shows that the Bejan number is consistently of lower magnitude for a Newtonian fluid compared to a Casson fluid.

Figures 13a-13b present the entropy lines for different values of β , Da , $\varepsilon_1\Theta^{-1}$ and Gr . In Fig. 13a, the variation of β is shown between (i) and (ii); & Da between (ii) and (iii). Similarly, the variation of control parameters $\varepsilon_1\Theta^{-1}$ & Gr is shown in Fig. 13b. From Fig. 13a [(i), (ii) & (iii)] it is seen that, the entropy lines becoming close to the hot wall as β or Da increases. Similarly, in Fig. 13b [(i) & (ii)] the entropy lines are observed to move away from the hot wall as $\varepsilon_1\Theta^{-1}$ increases. However in Fig. 13b [(ii) & (iii)] there is no substantial variation in entropy lines as the flow takes place from the hot wall to the cold wall with increasing values of Gr . The important observation from these figures is the entropy production occurs only in the neighbourhood of the hot cylindrical wall for all values of β , Da , Gr and $\varepsilon_1\Theta^{-1}$.

In the same way the Bejan lines for different values of control parameters are visualized in **Figs. 14a – 14b**. For all values of β , Da , Gr and $\varepsilon_1\Theta^{-1}$, it is observed that the variation of Bejan lines is confined to the proximity of the hot cylindrical wall only. From Fig. 14a it is seen that the Bejan lines approach closer to the hot wall with increasing values of β whereas they depart further from the all with increasing Da . Fig. 14a also indicates that the Be curves fluctuate in the rectangular region i.e., $0 \leq X \leq 1$, $2 \leq R \leq 3$. This fluctuation is greater for Da as compared to β . However in Fig. 14b this type of fluctuation is absent for Be curves when Grashof number, Gr

or $\varepsilon_1 \Theta^{-1}$ increase. Finally in Fig. 14b it is apparent that the Bejan lines move away from the hot wall as $\varepsilon_1 \Theta^{-1}$ or Gr increase.

4.4 Stream and heat functions

The fluid motion is simulated using the non-dimensional stream function ψ that satisfies the mass conservation (continuity) Eqn. (7). The relationship between U , V and ψ for two-dimensional incompressible flows is given by:

$$U = \frac{1}{R} \frac{\partial \psi}{\partial R} \quad \text{and} \quad V = -\frac{1}{R} \frac{\partial \psi}{\partial X} \quad (21)$$

This equation yields

$$\frac{\partial^2 \psi}{\partial X^2} + \frac{\partial^2 \psi}{\partial R^2} = U + R \frac{\partial U}{\partial R} - R \frac{\partial V}{\partial X} \quad (22)$$

Similarly the heat function Ω' for the temperature is defined as:

$$\frac{\partial \Omega'}{\partial x} = \rho r v c_p (T' - T'_\infty) - k r \frac{\partial T'}{\partial r} \quad (23a)$$

$$-\frac{1}{r} \frac{\partial \Omega'}{\partial r} = \rho u c_p (T' - T'_\infty) \quad (23b)$$

Clearly Ω' satisfies the time-independent state energy balance equation (4). The non-dimensional heat function $\Omega = \frac{\Omega'}{k(T'_0 - T'_\infty)r_0 Gr}$, renders the heat function dimensionless. It can be noted that the maximum value of this function equals the overall average heat transport coefficient on the hot wall [49, 51]. Equations (23a) and (23b) in terms of Ω can be re-written as:

$$\frac{\partial \Omega}{\partial X} = Pr(RV\theta) - R \frac{\partial \theta}{\partial R} \quad (24a)$$

$$-\frac{\partial \Omega}{\partial R} = Pr(RU\theta) \quad (24b)$$

Note that the above equations identically satisfy the time-independent state form of energy equation Eq. (9). Using Eqns. (23a, b), one can obtain the following Poisson equation which gives heat function field as:

$$\frac{\partial^2 \Omega}{\partial X^2} + \frac{\partial^2 \Omega}{\partial R^2} = Pr \left[R \frac{\partial(V\theta)}{\partial X} - R \frac{\partial(U\theta)}{\partial R} - U\theta \right] - R \frac{\partial^2 \theta}{\partial X \partial R} \quad (25)$$

Figures 15a - 15c illustrate the streamlines, isotherms and heatlines at the time-independent state for various values of β and Da , respectively. The values of ψ , θ and Ω , are calculated by second-order central differences. In each figure the variation of β is shown between (i) and (ii); similarly, Da between (ii) and (iii); and again (iii) and (iv) for Casson and Newtonian fluid ($\beta = \infty$) flows, respectively. The heatlines and isotherms occur very near to the hot cylindrical surface in comparison to the streamlines. From Fig. 15a [(i) & (ii)] it is observed that as Casson viscoplastic parameter, β , increases, the streamlines tend to gravitate closer to the hot wall. Fig. 15a [(ii) & (iii)] shows that the streamlines depart away from the hot wall as Da increases. It is also noticed that as Da increases the pattern of streamlines is transformed strongly. Similarly, from Fig. 15a [(iii) & (iv)] the streamlines are closer for the Newtonian fluid as compared to the Casson fluid. The streamlines are thicker around the leading edge of the cylinder as observed in Fig. 15a. Also, the heat transfer intensity from the wall to the Casson fluid is maximum for increasing values of X , and logically therefore decreases as X decreases. From Fig. 15b it is evident that isotherms move somewhat closer to the hot cylindrical wall as Da or β increases. Also, as β or Da are increased, the variation in isotherms is minimized. It is also important to highlight that isotherms represent the temperature levels in the domain, but they are weak and inadequate tools for detailed heat transfer visualization and analysis. Hence the fluid flow and heat transfer visualization can be done with the help of heatlines which is shown in Fig. 15c. The heatlines are observed to have a similar trend to that of isotherms. The heatlines show the heat extraction from the hot cylindrical surface. The heatlines indicate bordered corridors and are a useful tool for heat transfer visualization and analysis, providing much more information than isotherms. Heatlines are found to migrate slightly towards the hot wall as Da increases and the reverse trend is computed with increasing seen β . Also, as β or Da increases, the maximum value of Ω increases, since \overline{Nu} increases on the hot cylindrical surface as tabulated in **Table 4**. The values of heat function Ω for the Newtonian fluid exceed those for the Casson fluid. Furthermore the deviation of heatlines from the hot cylindrical wall for a Newtonian fluid ($\beta = \infty$) is less pronounced than that computed for the Casson fluid. Finally, it is concluded that the variation in heatlines is intensified in the proximity of the hot cylindrical wall compared to that of streamlines and isotherms.

4.5 Comparison between Casson and Newtonian fluid flows

Table 3 documents the differences between Casson and Newtonian fluid flows for the flow-field variables with their temporal peak and the time-independent state values for Da , β , Gr and $\varepsilon_1 \Theta^{-1}$. Table 3a represents Casson fluid and Table 3b corresponds to a Newtonian fluid. With increasing Da and β , the time required for U and θ variables to attain the temporal peak for the Casson fluid is higher than for Newtonian fluid and the reverse trend is observed for Ns and Be . Similarly, for every Da and β , the steady-state time for U , θ , Ns and Be is greater for Newtonian fluid as compared to that of Casson fluid. Also, for each Da and β , the peak velocity values occur at $X = 1.0$, and these values for Casson fluid are smaller compared with those of Newtonian fluid.

Table 4 tabulates the differences between the Casson fluid and Newtonian fluid for average momentum and heat transport coefficients with various Da and β . Table 4a corresponds to the Casson fluid and Table 4b to a Newtonian fluid. From Tables 4a and 4b, it is observed that the values of the skin-friction coefficient of a Casson fluid are larger compared to the Newtonian fluid. However the opposite trend is noted for average Nusselt number. Thus, the characteristics of average momentum and heat transport coefficients of Casson fluid significantly vary from that of the Newtonian fluid.

Figs. 16a and 16b illustrate the U and θ contours for Casson and Newtonian fluid flows, respectively. At any given point of location in the 2-dimensional rectangular computational domain (X, R) except at the boundary points ($X = 0, R = 1$ & $R = 20$), the velocity of the Casson fluid flow is observed to be smaller than for a Newtonian fluid. However for the temperature profiles, the reverse trend is noticed. Also, the time-independent state velocity and temperature contours for a Casson fluid are slightly different with thicker hydrodynamic and thermal boundary layers than those of a Newtonian fluid.

5. CONCLUDING REMARKS

The entropy generation minimization along with Bejan's heatline visualization technique have been employed in this article to examine heat transfer optimization in time-dependent free convective Casson fluid boundary layer flow from an isothermal cylinder embedded in a porous medium. The Crank-Nicolson technique has been applied to solve the normalized, partial

differential conservation equations for momentum and energy conservation. Bejan's heat flow concept includes the heatline plots. The physical characteristics of heatlines are immensely beneficial in visualizing heat transfer in the two dimensional domain. Also in a given rectangular computational domain, the heatlines provide a powerful method for evaluating the heat transfer rate at all levels. A non-dimensional heat function is employed which is closely related to the average heat transport coefficient on the hot cylindrical wall and characterizes the overall heat transfer rate process from the hot to the cold wall. Also, the entropy generation and Bejan numbers are derived and evaluated with the help of flow-field variables. The influences of Casson fluid parameter and Darcy parameter on flow profiles along with average momentum and heat transport coefficients are discussed. Furthermore the effect of Casson fluid parameter, Darcy number, group parameter and Grashof number on entropy generation and Bejan numbers are analyzed. The pertinent deductions from the present study may be summarized as follows:

1. The time taken to achieve the steady-state increases as Casson viscoplastic fluid parameter increases, and the contrary trend is computed with increasing Darcy number.
2. The velocity increases and temperature decreases with rising values of Casson viscoplastic fluid parameter or Darcy number. Also averaged momentum transport coefficient (skin friction) is increased with greater values of Darcy number whereas it is decreased with increasing Casson viscoplastic fluid parameter. Similarly, the averaged heat transport coefficient (Nusselt number) is observed to increase with increasing values of Casson viscoplastic fluid parameter or Darcy number.
3. Entropy heat generation parameter and Bejan number increase with increasing values of Casson viscoplastic fluid parameter, Darcy number, Grashof number or group parameter.
4. The time to attain temporal peak for entropy generation decrease with increasing Casson viscoplastic fluid parameter or Darcy number, Grashof number or group parameter.
5. The time to accomplish the steady-state for the velocity, temperature, entropy generation and Bejan number increase with increasing viscoplastic fluid parameter, Darcy number or group parameter whereas they are reduced with increasing Grashof (free convection) number.

6. The transient and steady-state results of flow variables, average heat and momentum transport coefficients, entropy production, Bejan number for *non-Newtonian Casson fluid* differ significantly from those computed for a *Newtonian fluid*.
7. Flow visualization indicates that the streamlines occur in the entire two-dimensional domain, while the isotherms and heatlines exist in a finite region which is observed adjacent to the hot cylindrical wall.

The present study has provided some interesting insights in entropy generation associated with non-Newtonian thermal convection boundary layer flows in porous media. Future studies will consider *thermal stratification* effects in porous media [58] and alternative (e.g. Oldroyd-B viscoelastic) rheological models [59] and also *nanofluids* [60] and will be communicated imminently.

ACKNOWLEDGEMENTS

The third author wishes to thank DST-INSPIRE (Code No. IF160028) for the grant of research fellowship and to Central University of Karnataka for providing the research facilities.

REFERENCES

1. Sparrow, E. M. and Gregg, J. L.: Laminar free convection heat transfer from the outer surface of a vertical circular cylinder. *ASME Journal of Heat Transfer* 78(8), 1823-1829 (1956).
2. Lee, H. R., Chen, T. S. and Armaly, B. F.: Natural convection along slender vertical cylinders with variable surface temperature. *ASME Journal of Heat Transfer* 110, 103-108(1988).
3. Rani, H. P. and Reddy, G. J.: Soret and Dufour effects on transient double diffusive free convection of couple-stress fluid past a vertical cylinder. *Journal of Applied Fluid Mechanics* 6(4), 545-554 (2013).

4. Hirschhorn, J., Madsen, M., Mastroberardino, A. and Siddique, J. I.: Magnetohydrodynamic boundary layer slip flow and heat transfer of power law fluid over a flat plate. *Journal of Applied Fluid Mechanics* 9(1), 11-17 (2016).
5. Makanda Gilbert, Shaw Sachin, Sibanda Precious. Diffusion of chemically reactive species in Casson fluid flow over an unsteady stretching surface in porous medium in the presence of a magnetic field. *Math Probl Eng* 2014, (2014). Article Id 724596.
6. Dash, R. K., Mehta, K. N. and Jayaraman, G.: Casson fluid flow in a pipe filled with a homogeneous porous medium. *International Journal of Engineering Science* 34, 1145-1156 (1996).
7. Casson, N.: A flow equation for pigment oil suspensions of the printing ink type. In: *Rheology of disperse systems. Mill CC (Ed.) Pergamon Press, Oxford* 84–102. (1959).
8. Walwander WP, Chen TY, Cala DF. An approximate Casson fluid model for tube flow of blood, *Biorheology*, 12:111 (1975).
9. Copley, A.L. In *Flow properties of blood and other biological systems. Edited by A.L. Copley and G. Stainsly*. Pergamon Press, Oxford. (1960).
10. Venkatesan, J., Sankar, D.S., Hemalatha, K. and Yatim, Y.: Mathematical analysis of Casson fluid model for blood rheology in stenosed narrow arteries. *Journal of Applied Mathematics*, Volume 2013, Article ID 583809 (2013).
11. Abbas, Z., Sheikh, M. and Motsa, S. S.: Numerical solution of binary chemical reaction on stagnation point flow of Casson fluid over a stretching/shrinking sheet with thermal radiation. *Energy* 95, 12-20 (2016).
12. Mustafa, M., Hayat, T., Pop, I. and Hendi, A.: Stagnation-point flow and heat transfer of a Casson fluid towards a stretching sheet. *Zeitschrift fur Naturforschung* 67, 70-76 (2012).
13. Mythili, D. and Sivaraj, R.: Influence of higher order chemical reaction and nonuniform heat source/sink on Casson fluid flow over a vertical cone and flat plate. *Journal of Molecular Liquids* 216, 466-475 (2016).
14. Das, M., Mahato, R. and Nandkeolyar, R.: Newtonian heating effect on unsteady hydromagnetic Casson fluid flow past a flat plate with heat and mass transfer. *Alexandria Engineering Journal* 54, 871-879 (2015).

15. Nadeem, S., Haq, R. U. and Lee, C.: Magnetohydrodynamic flow of a Casson fluid over an exponentially shrinking sheet. *Scientia Iranica* 19, 1550-1553 (2012).
16. Raju, C. S. K., Sandeep, N., Sugunamma, V., Babu, M. J. and Reddy, J. R.: Heat and mass transfer in magnetohydrodynamic Casson fluid over an exponentially permeable stretching surface. *Engineering Science and Technology-An International Journal* 19, 45-52 (2016).
17. Bejan, A.: The concept of irreversibility in heat exchanger design: counterflow heat exchangers for gas-to-gas applications. *ASME Journal of Heat Transfer* 99, 374-380 (1977).
18. Giangaspero, G. and Sciubba, E: Application of the entropy generation minimization method to a solar heat exchanger: A pseudo-optimization design process based on the analysis of the local entropy generation maps. *Energy* 58, 52-65 (2013).
19. Badescu, V.: Optimal paths for minimizing lost available work during usual heat transfer processes. *Journal of Non-Equilibrium Thermodynamics* 29, 53-73 (2004).
20. Kockum, H. and Jernqvist, A: Entropy generation in multifield flows: Equations and Examples of Applications. *Trans IChemE* 76, 212-222 (1998).
21. Bejan, A.: A study of entropy generation in fundamental convective heat transfer. *ASME Journal of Heat Transfer* 101, 718-725 (1979).
22. Bejan, A.: Second law analysis in heat transfer. *Energy* 5, 720-732 (1980).
23. Bejan, A.: Second law analysis in heat transfer and thermal design. *Advances in Heat Transfer* 15, 1-58 (1982).
24. Mahian, O., H. Oztop, Ioan Pop, Shohel Mahmud, Somchai Wongwises: Entropy generation between two vertical cylinders in the presence of MHD flow subjected to constant wall temperature. *International Communications in Heat and Mass Transfer* 44, 87-92 (2013).
25. Butt, A.S., A. Ali: Entropy analysis of magnetohydrodynamic flow and heat-transfer due to a stretching cylinder. *Journal of Taiwan Institute of Chemical Engineers* 45, 780-786 (2014).
26. Sufian Munawar, Asif Ali, A. Mehmood: Thermal analysis of the flow over an oscillatory stretching cylinder. *Physica Scripta* 86(2), 065-401 (2012).

27. Butt, A.S., A. Ali, A. Mehmood: Numerical investigation of magnetic field effects on entropy generation in viscous flow over a stretching cylinder embedded in a porous medium. *Energy* 99, 237-249 (2016).
28. Bassam A.K. Abu-Hijleh: Natural convection heat transfer and entropy generation from a horizontal cylinder with baffles. *ASME Journal of Heat Transfer* 122(4), 679-692 (2000).
29. Bassam A.K. Abu-Hijleh: Natural convection and entropy generation from a cylinder with high conductivity fins. *Numerical Heat Transfer, Part A* 39, 405-432 (2001).
30. Bassam A.K. Abu-Hijleh, B.A/K.: Entropy generation due to cross-flow heat transfer from a cylinder covered with an orthotropic porous layer. *Heat and Mass Transfer* 39, 27-40 (2002).
31. Mirzazadeh M, Shafaei A, Rashidi F: Entropy analysis for non-linear visco-elastic fluid in concentric rotating cylinders. *International Journal of Thermal Sciences* 47(12), 1701-1711(2008).
32. Mahian O, Mahmud S, Heris SZ.: Analysis of entropy generation between co-rotating cylinders using nanofluid. *Energy* 44(1), 438-446 (2012).
33. Bassam A.K. Abu-Hijleh, Waleed N. Heilen: Entropy generation due to laminar natural convection over a heated rotating cylinder. *International Journal of Heat and Mass Transfer* 42, 4225-4233(1999).
34. Jia Qing, Muhammad Mubashir Bhatti , Munawwar Ali Abbas, Mohammad Mehdi Rashidi and Mohamed El-Sayed Ali: Entropy generation on MHD Casson nano fluid flow over a porous stretching/shrinking surface. *Entropy* 18(4), 1-14 (2016).
35. Sheffield, R.E. and Metzner, A.B.: Flows of nonlinear fluids through porous media, *AIChE J.*, 22, 736 (1976).
36. Kakac, S., Kilkis, B., Kulacki, F. and Arine, F. : *Convective Heat and Mass Transfer in Porous Media*, Kluwer, Netherlands (1991).
37. Nield, D.A. and Bejan, A.: *Convection in Porous Media*, Springer-Verlag, New York (1999).
38. Nandeppanavar, M., Mahantesh, M., Subhas Abel, K. and Vajravelu.: Flow and heat transfer characteristics of a viscoelastic fluid in a porous medium over an impermeable stretching sheet with viscous dissipation. *Int. J. Heat Mass Transfer.*, 53, 4707-4713 (2010).

39. M.M. Rashidi, T. Hayat, M. Keimanesh, and H. Yousefian.: A study on heat transfer in a second-grade fluid through a porous medium with the modified differential transform method. *Heat Transfer-Asian Research*, 42 (1) (2013).
40. Adnan Saeed Butt, Sufian Munawar, Ahmer Mehmood and Asif Ali.: Effect of Viscoelasticity on Entropy generation in a porous medium over a stretching plate. *World Applied Sciences Journal* 17 (4): 516-523 (2012).
41. Bég, O Anwar, H S Takhar, R Bhargava, S Rawat and V R Prasad.: Numerical study of heat transfer of a third grade viscoelastic fluid in non-Darcy porous media with thermophysical effects. *Physica Scripta*. 77 (2008) 065402.
42. Ramachandra Prasad, V., Abdul Gaffar, S., Keshava Reddy, E., and Anwar Bég, O. : Numerical study of Non-Newtonian boundary layer flow of Jeffreys fluid past a vertical porous plate in a Non-Darcy porous medium. *International Journal for Computational Methods in Engineering Science and Mechanics* 15, 372–389 (2014).
43. Srinivas,J., Ramana Murthy,J.V., and Sai, K.S.: Entropy generation analysis of the flow of two immiscible couple stress fluids between two porous beds. *Computational Thermal Sciences* 7(2), 123–137 (2015).
44. Asma Khalid, Ilyas Khan, Arshad Khan and Sharidan Shafie: Unsteady MHD free convection flow of Casson fluid past over an oscillating vertical plate embedded in a porous medium. *Engineering Science and Technology, an International Journal* 18(3), 309-317 (2015).
45. Ramachandra Prasad, V., Subba Rao, A., and Anwar Bég, O. : Flow and heat transfer of Casson fluid from a horizontal circular cylinder with partial slip in non-Darcy porous medium. *Journal of Applied and Computational Mathematics* 2(2), 1-12 (2013).
46. Hari R. Kataria, Harshad R. Patel.: Radiation and chemical reaction effects on MHD Casson fluid flow past an oscillating vertical plate embedded in porous medium. *Alexandria Engineering Journal* (2016) 55, 583–595.
47. S. A. Shehzad, T. Hayat and A. Alsaedi.: Three-dimensional MHD flow of Casson fluid in porous medium with heat generation. *Journal of Applied Fluid Mechanics*, 9, 215-223 (2016).
48. F. Mabood, R. G. Abdel-Rahman, and G. Lorenzini.: Effect of melting heat transfer and thermal radiation on Casson fluid flow in porous medium over moving

- surface with magnetohydrodynamics. *Journal of Engineering Thermophysics*, 25, 536–547 (2016).
49. Kimura, S. and Bejan, A.: The heatline visualization of convective heat transfer. *ASME Journal of Heat Transfer* 105, 916-919 (1983).
50. Bejan, A.: *Convection Heat Transfer*. 1st ed. New York: John Wiley and Sons.(1984).
51. Aggarwal, S. and Manhapra, A.: Use of heatlines for unsteady buoyancy-driven flow in a cylindrical enclosure. *ASME Journal of Heat Transfer* 111, 576-578 (1989).
52. Rani, H. P. and Reddy, G. J.: Heatline visualization for conjugate heat transfer of a couple stress fluid from a vertical slender hollow cylinder. *International Communications in Heat and Mass Transfer* 48, 46-52 (2013).
53. Rani, H. P., Reddy, G. J., Kim, C. N. and Rameshwar, Y.: Transient couple stress fluid past a vertical cylinder with bejans heat and mass flow visualization for steadystate. *ASME Journal of Heat Transfer* 137, 032501-12 (2015).
54. Das, D. and Basak, T.: Analysis of average Nusselt numbers at various zones for heat flow visualizations during natural convection within enclosures (square vs triangular) involving discrete heaters. *International Communications in Heat and Mass Transfer* 75, 303- 310 (2016).
55. Morega, A.: The heat function approach to the thermomagnetic convection of electroconductive melts. *Revue roumaine des Sciences Techniques. Electrotechnique et Energetique* 33, 359-368 (1988).
56. Rani, H. P., Janardhana Reddy, G. and Kim, C.N.: Transient analysis of diffusive chemical reactive species for couple stress fluid flow over vertical cylinder. *Applied Mathematics and Mechanics English Edition* 34, 985-1000 (2013).
57. Bejan, A.: *Entropy Generation Minimization*. CRC Press, New York, USA (1996).
58. Bég, O. Anwar, J. Zueco and H.S. Takhar, Laminar free convection from a continuously moving vertical surface in a thermally-stratified, non-Darcian high-porosity medium: Network numerical study, *Int. Comm. Heat Mass Transfer*, 35, 7, 810-816 (2008).
59. Norouzi, M., M. Davoodi and O. Anwar Bég, An analytical solution for convective heat transfer of viscoelastic flows in rotating curved pipes, *Int. J. Thermal Sciences*, 90, 90-111 (2015).
-

60. Bég, O. Anwar, M. F. M. Basir, M.J. Uddin, and A. I. M. Ismail, Numerical study of slip effects on asymmetric bioconvective nanofluid flow in a porous microchannel with an expanding/contracting upper wall using Buongiorno's model, *J. Mechanics in Medicine and Biology*, 17 (5) 1750059 (28 pages) (2017).
-

TABLES

Grid size	Average skin-friction coefficient (\bar{C}_f) for $Pr = 0.71$, $Da = 5.0$ and $\beta = 1.0$.	Average Nusselt number (\bar{Nu}) for $Pr = 0.71$, $Da = 5.0$ and $\beta = 1.0$.
25 X 125	1.0928050	0.7903369
50 X 250	1.0930550	0.7913445
100 X 500	1.0985270	0.7920794
200 X 1000	1.0985310	0.7920817

Table 1. Grid independence test for selecting mesh size

Time step size (Δt)	Average skin-friction coefficient (\overline{C}_f) for $Pr = 0.71$, $Da = 5.0$ and $\beta = 1.0$.	Average Nusselt number (\overline{Nu}) for $Pr = 0.71$, $Da = 5.0$ and $\beta = 1.0$.
0.5	1.0986110	0.7922722
0.1	1.0986430	0.7922800
0.08	1.0986480	0.7922805
0.05	1.0985970	0.7922302
0.02	1.0985480	0.7921695
0.01	1.0985270	0.7920794

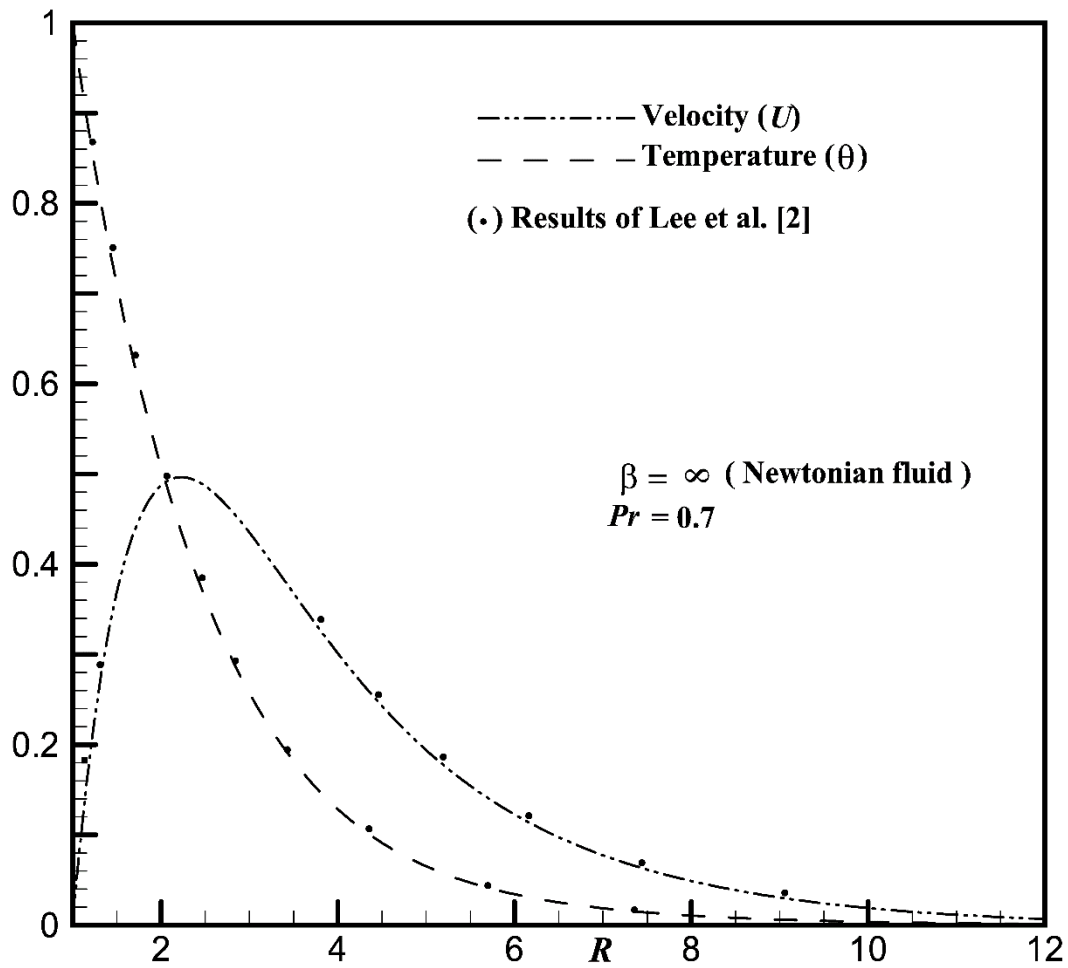
Table 2. Grid independence test for selecting time step size.

Table 3. The time required for various variables U , θ , Ns & Be to attain the temporal peak and the time-independent state; the peak velocity for various β , Da , Gr and $\varepsilon_1\theta^{-1}$ with $Pr = 0.71$ for (a) Casson fluid; & (b) Newtonian fluid.

β ($Gr=1.0, \varepsilon_1\theta^{-1}=0.1$)	Da	Temporal peak time (t) of				Steady-state time (t)	Peak value at $X = 1.0$		
		$U(1, 2.02)$	$\theta(1, 1.53)$	$Ns(1, 2.40)$	$Be(1, 2.40)$		U	Ns	Be
(a) Casson fluid									
0.5	5.0	6.63	6.31	7.46	6.59	11.80	0.3065	0.4577	0.0798
1.0	5.0	5.93	5.62	6.79	5.90	11.90	0.3538	0.4904	0.0861
1.5	5.0	5.66	5.35	6.57	5.64	12.14	0.3765	0.5050	0.0889
2.0	5.0	5.51	5.20	6.50	5.50	12.26	0.3900	0.5134	0.0905
1.0	1.2	7.04	6.75	7.83	7.04	12.99	0.2667	0.3958	0.0569
1.0	1.4	6.81	6.52	7.64	6.81	12.64	0.2795	0.4098	0.0609
1.0	1.8	6.52	6.22	7.38	6.51	12.18	0.2988	0.4309	0.0671
1.0	2.2	6.34	6.05	7.21	6.34	11.95	0.3126	0.4458	0.0717
Gr $\varepsilon_1\theta^{-1}$ ($\beta=1.0, Da=5.0$)									
1	0.1			6.79	5.90	11.80		0.4577	0.0861
2	0.1			6.68	5.90	11.90		0.4904	0.3445
3	0.1			6.41	5.90	12.14		0.5050	0.7751
4	0.1			6.18	5.90	12.26		0.5134	1.3779
5	0.1			6.06	5.90	12.99		0.3958	2.1530
1	1.0			6.37	5.90	12.64		0.4098	0.8612
1	3.0			6.03	5.90	12.18		0.4309	2.5836
1	5.0			5.97	5.90	11.95		0.4458	4.3060
1	7.0			5.95	5.90	12.18		0.4309	6.0285
1	9.0			5.94	5.90	11.95		0.4458	7.7509
(b) Newtonian fluid									
β	Da								
∞	1.2	5.95	5.67	6.72	5.95	13.30	0.3292	0.4296	0.0614
∞	1.4	5.75	5.46	6.62	5.75	13.07	0.3466	0.4470	0.0662
∞	2.2	5.35	5.05	6.56	5.35	12.67	0.3906	0.4913	0.0792
∞	5.0	5.00	4.69	5.89	5.02	12.82	0.4945	0.5966	0.1144

Table 4. Comparison between (a) Casson fluid and (b) Newtonian fluid flows for various values of β and Da with respect to the average values of \overline{C}_f and \overline{Nu} with $Pr = 0.71$.

β	Da	\overline{C}_f	\overline{Nu}
(a)			
0.5	1.2	1.1139	0.7203
0.5	5.0	1.2850	0.7622
1.0	5.0	1.0985	0.7920
1.5	5.0	1.0228	0.8052
2.0	5.0	0.9813	0.8127
5.0	1.2	0.7672	0.7764
5.0	5.0	0.8981	0.8283
1.0	1.2	0.9461	0.7458
1.0	1.4	0.9701	0.7535
1.0	1.8	1.0051	0.7645
1.0	2.2	1.0293	0.7719
(b)			
∞	1.2	0.7111	0.7869
∞	1.4	0.7308	0.7961
∞	2.2	0.7792	0.8176
∞	5.0	0.8349	0.8407

Fig. 1. Schematic of the investigated problem.

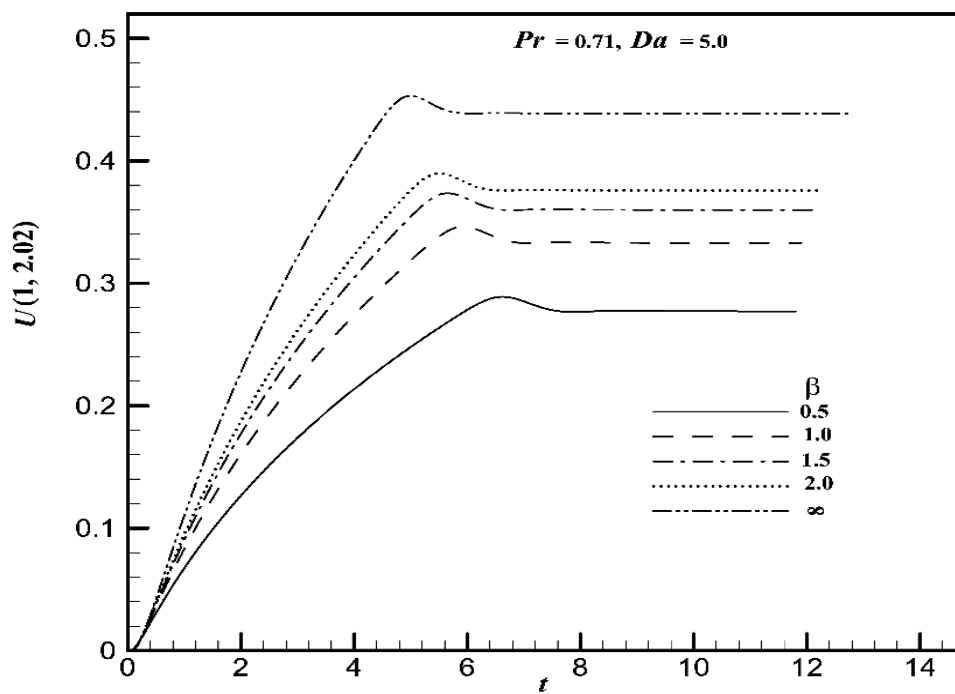
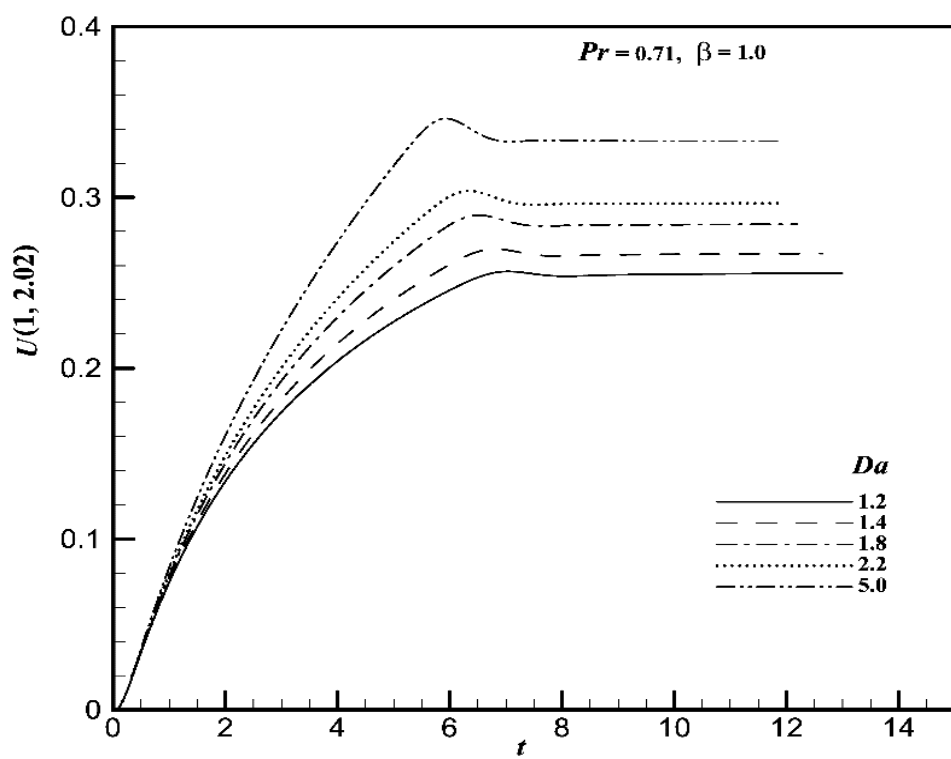


Fig. 2. Comparison of the velocity and temperature profiles.

profiles.

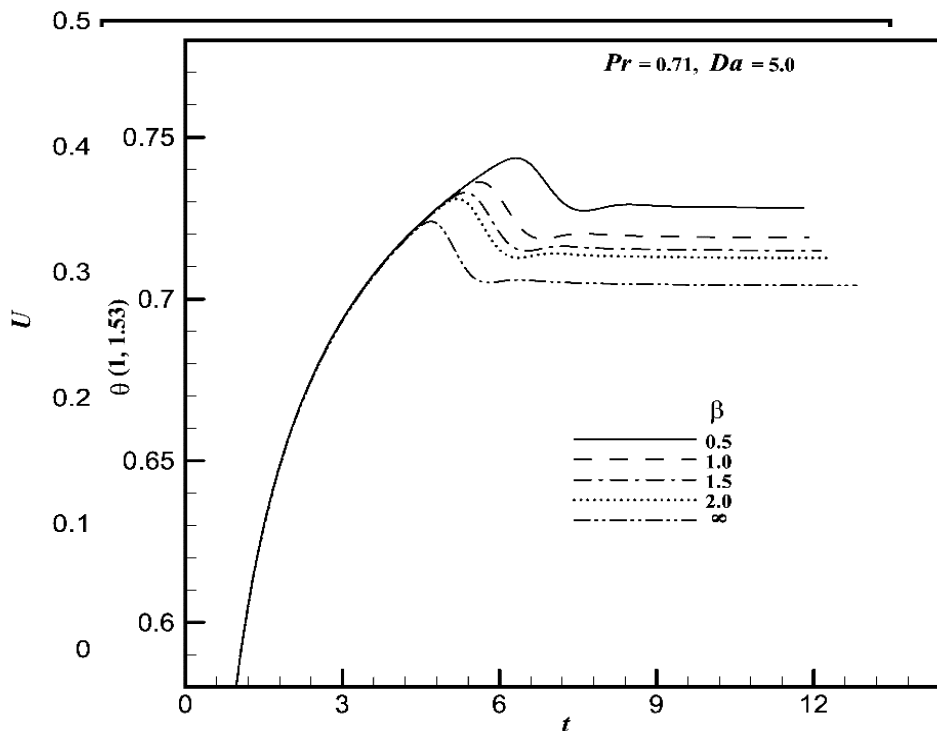
(3a)



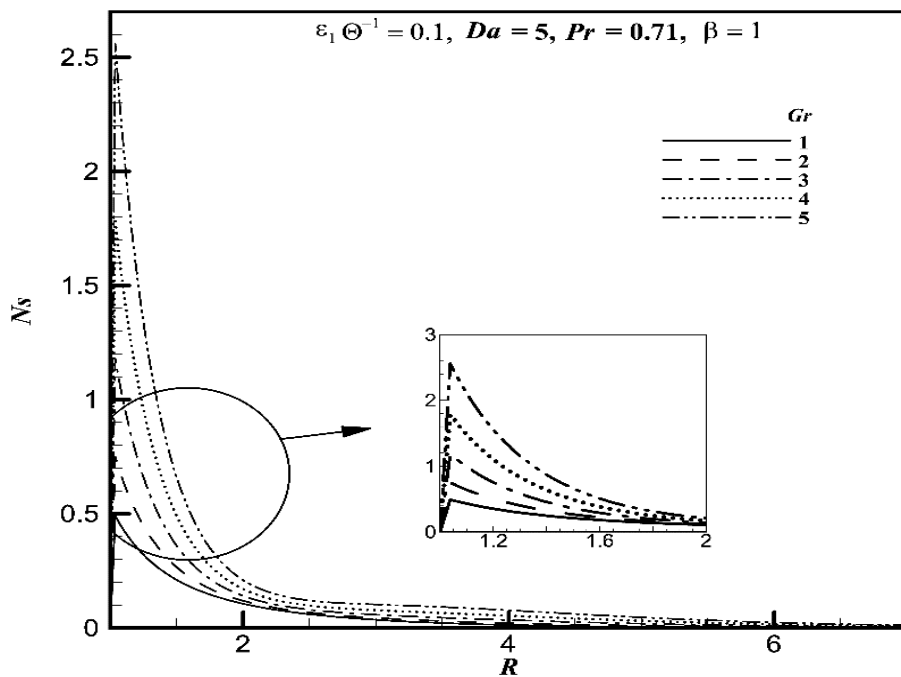
(3b)

Fig.3.

versus
the
2.02)
effect
(b)



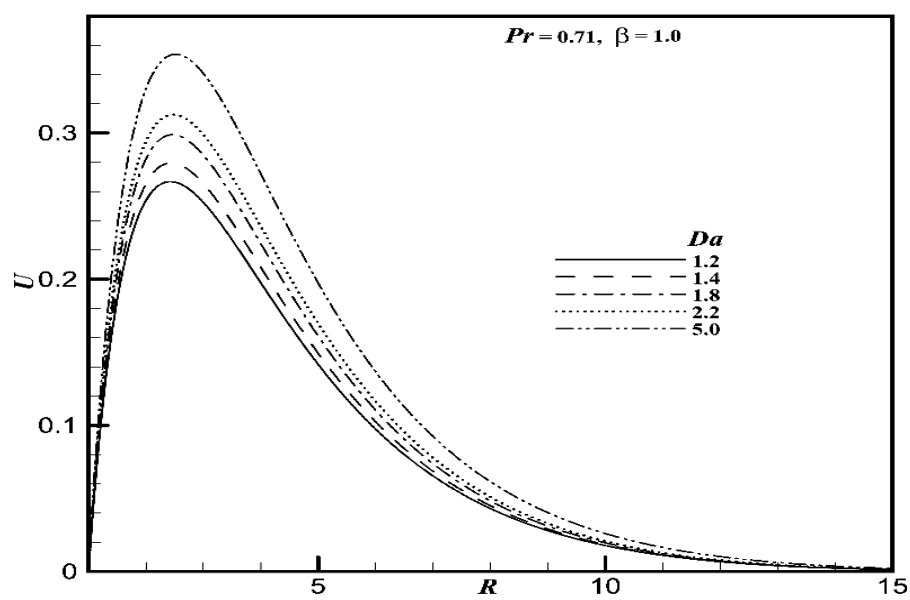
Time-
dependent
velocity
profile (U)
time (t) at
point (1,
for the
of (a) β ; &
 Da .



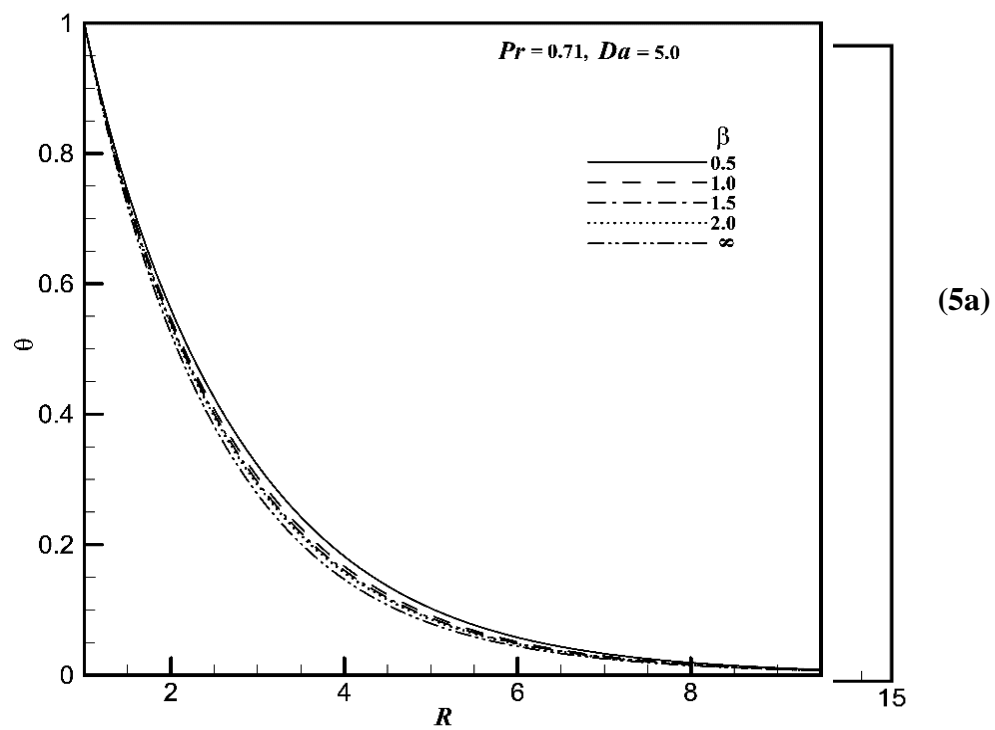
(4a)

(4b)

Fig. 4.
time-
state
(U)
1.0 for
 β ; &



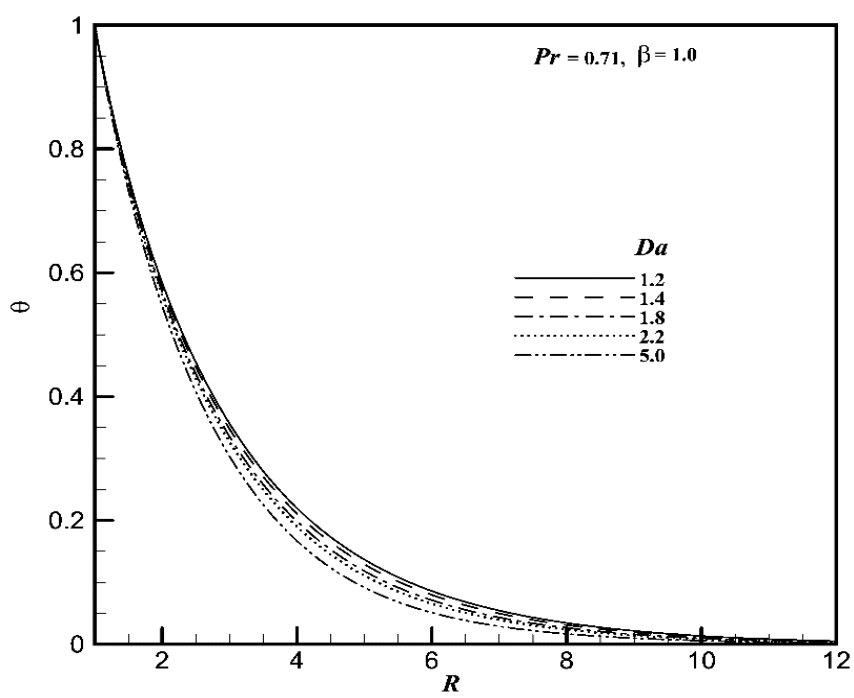
Simulated
independent
velocity profile
versus R at $X =$
the effect of (a)
(b) Da .



(5b)

Fig. 5. Simulated time-dependent temperature profile (θ) versus time (t) at the point (1, 1.53) for the effect of **(a)** β ; & **(b)** Da .

(6a)



(6b)

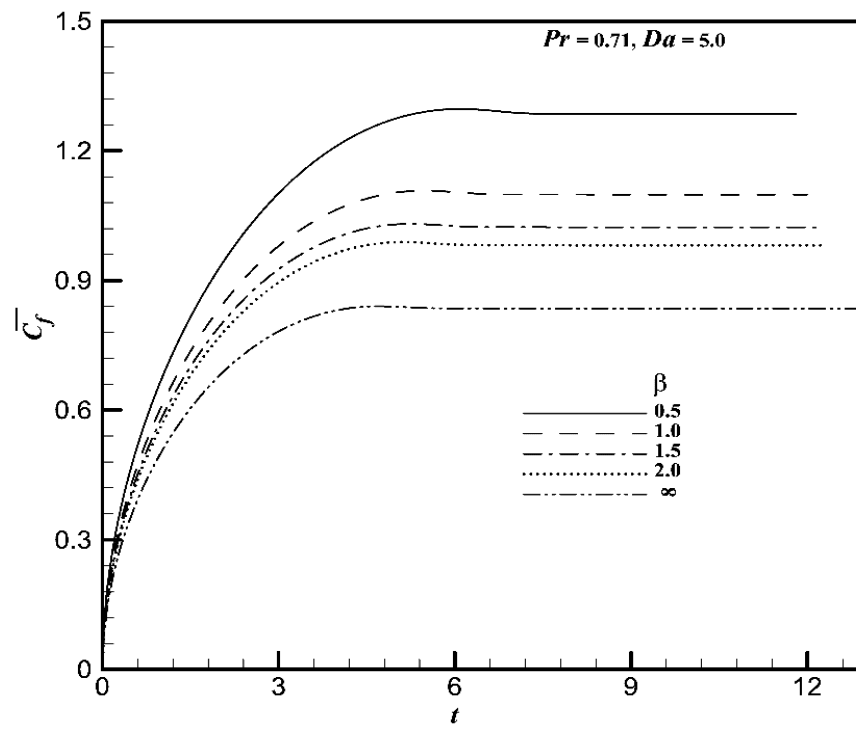


Fig. 6. Time-independent state temperature profile (θ) versus R at $X = 1.0$ for the effect of (a) β ; & (b) Da .

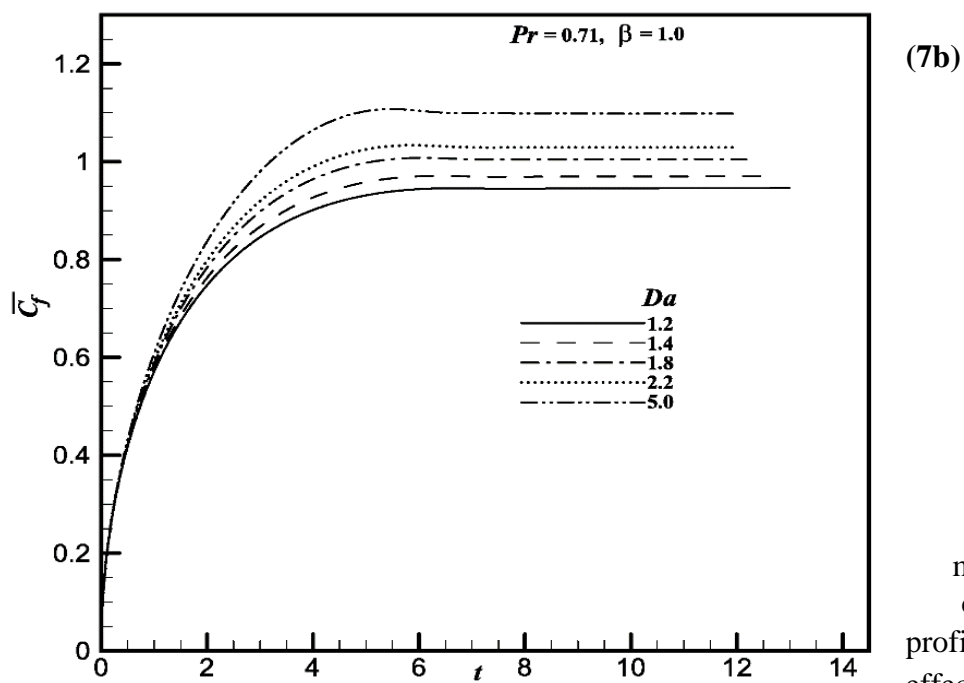
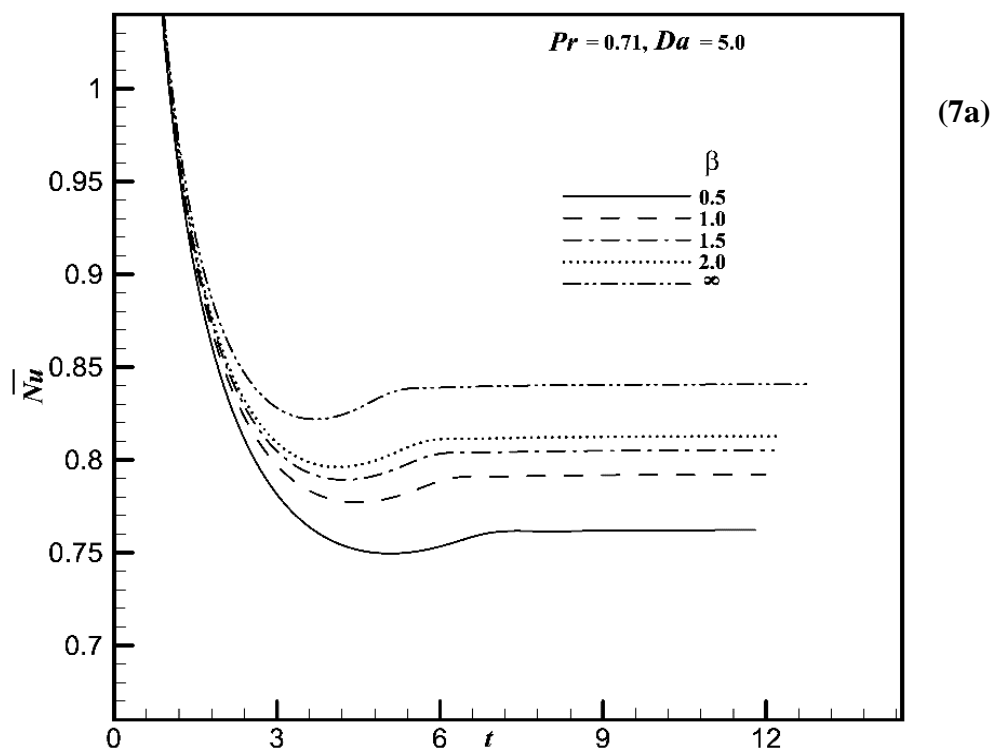


Fig. 7.
transport
(\bar{C}_f)
 t for the
& (b)

Average
momentum
coefficient
profile against
effect of (a) β ;
 Da .

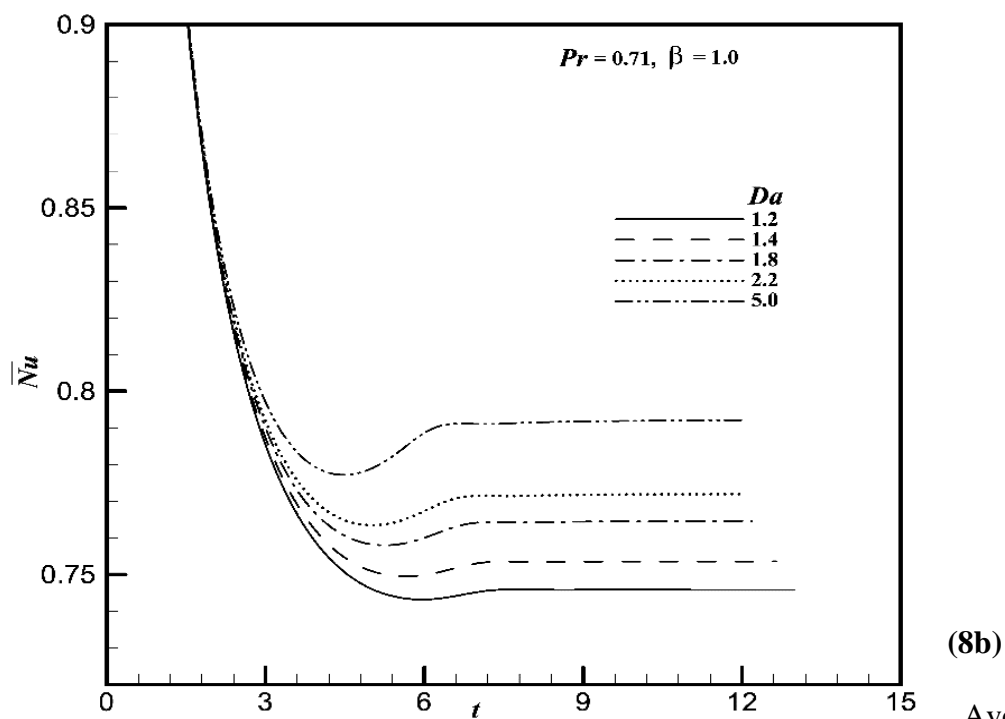
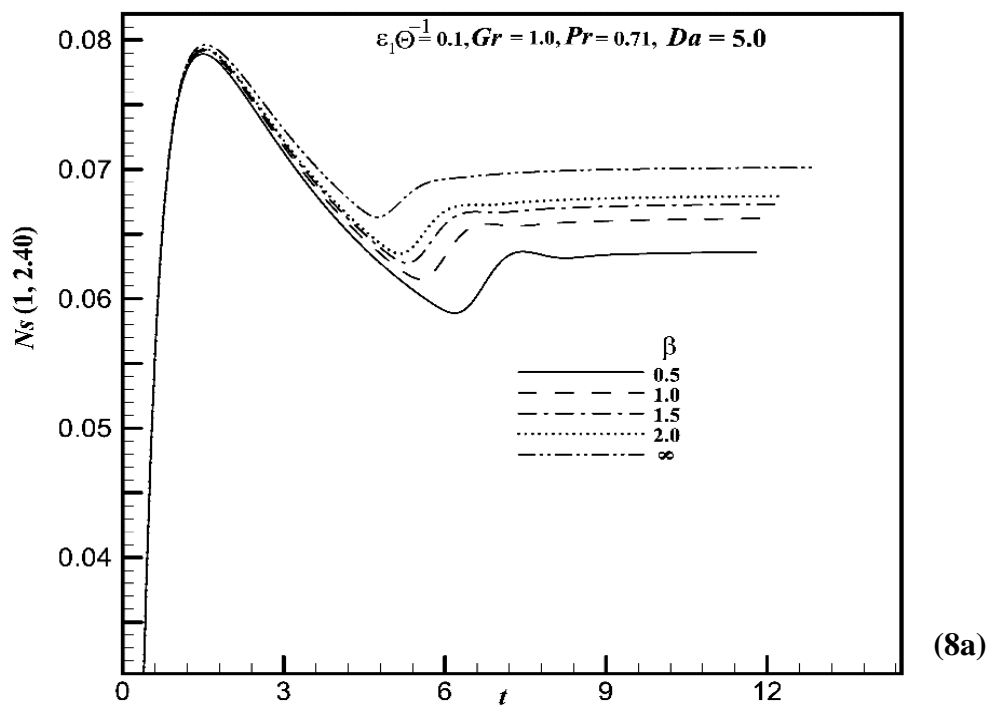
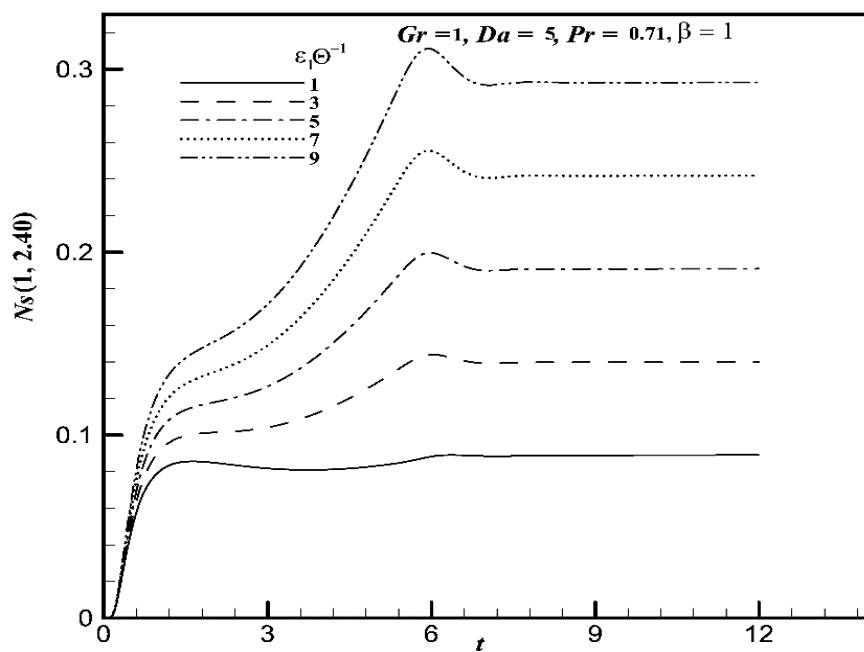
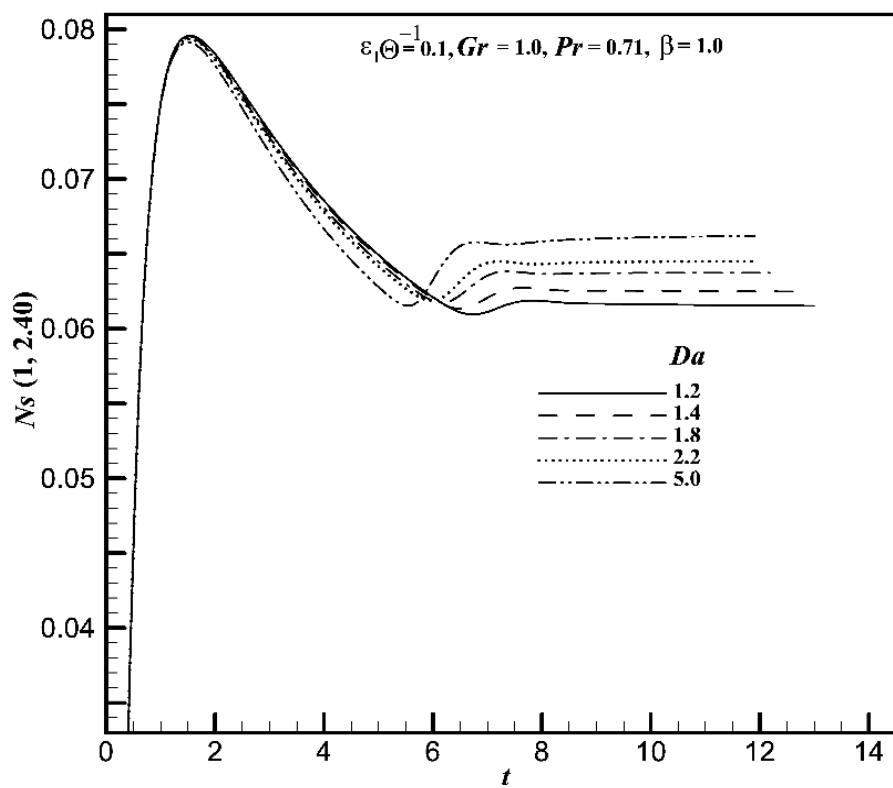


Fig. 8. heat coefficient (\bar{Nu}) profile against t for the effect of (a) β ; & (b) Da .

Average transport

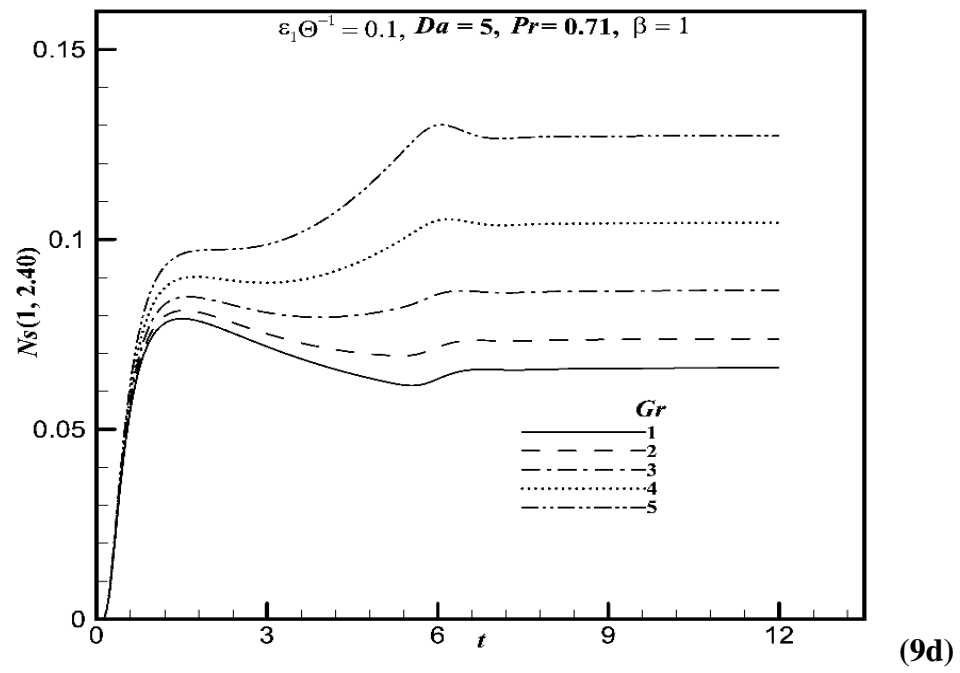


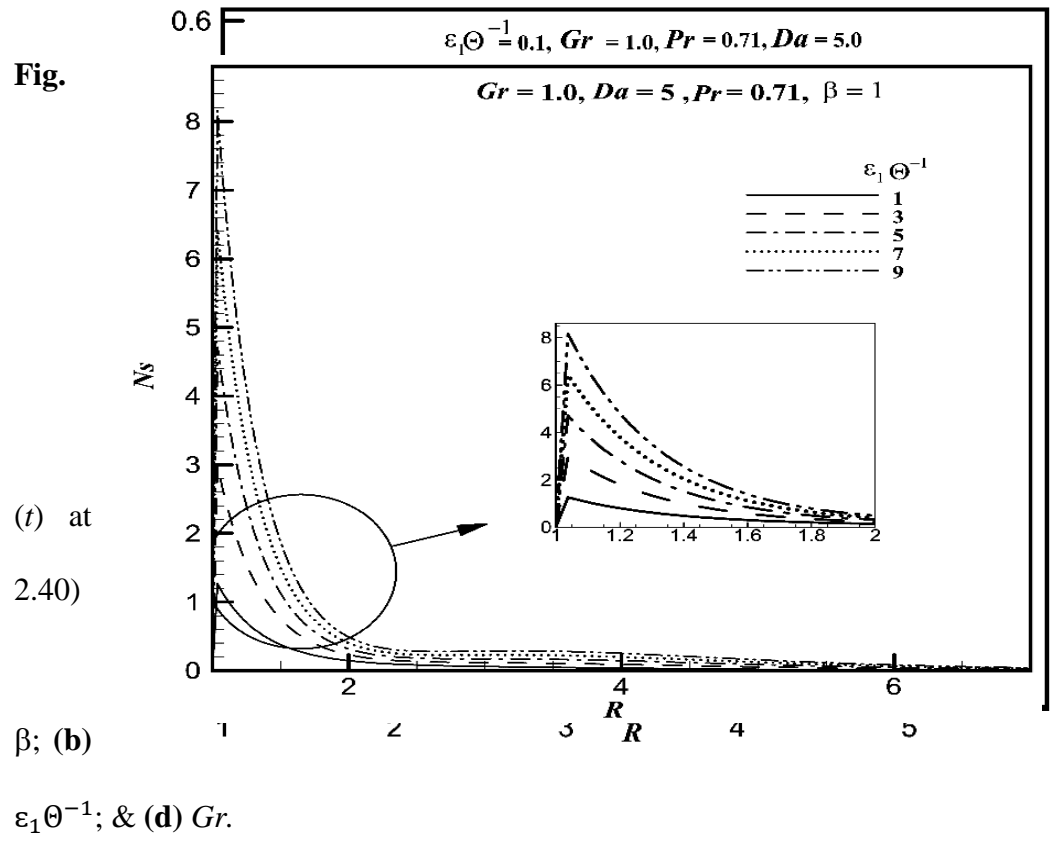
(9a)



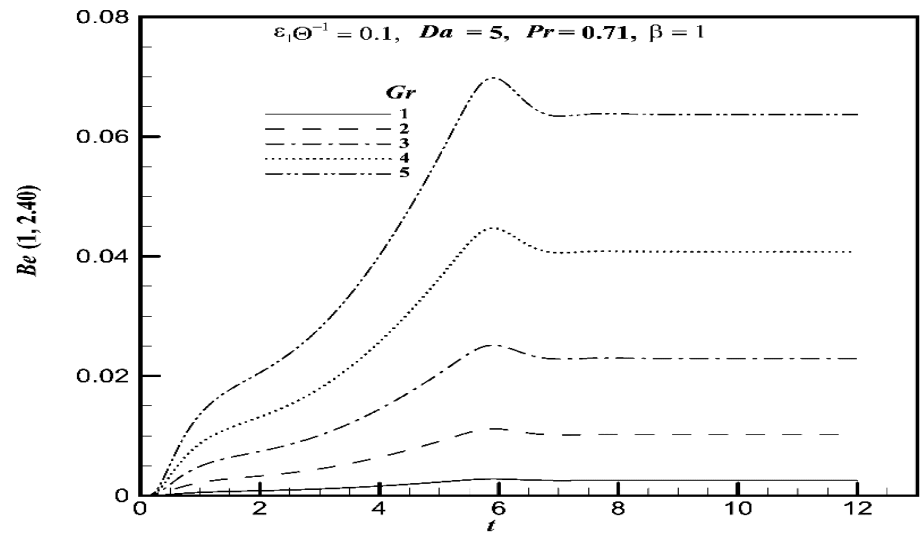
(9b)

(9c)

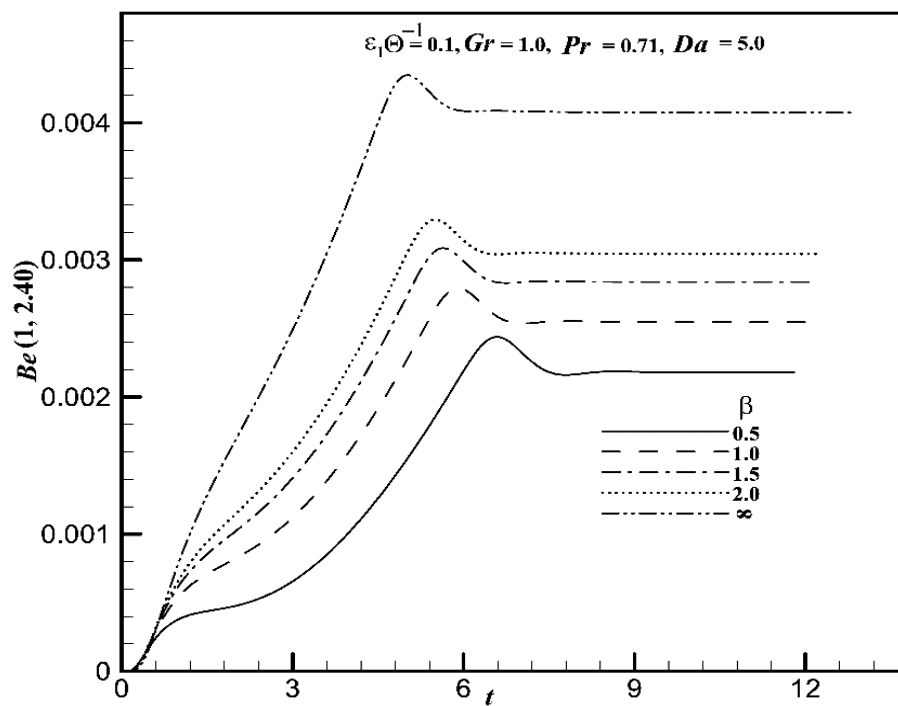




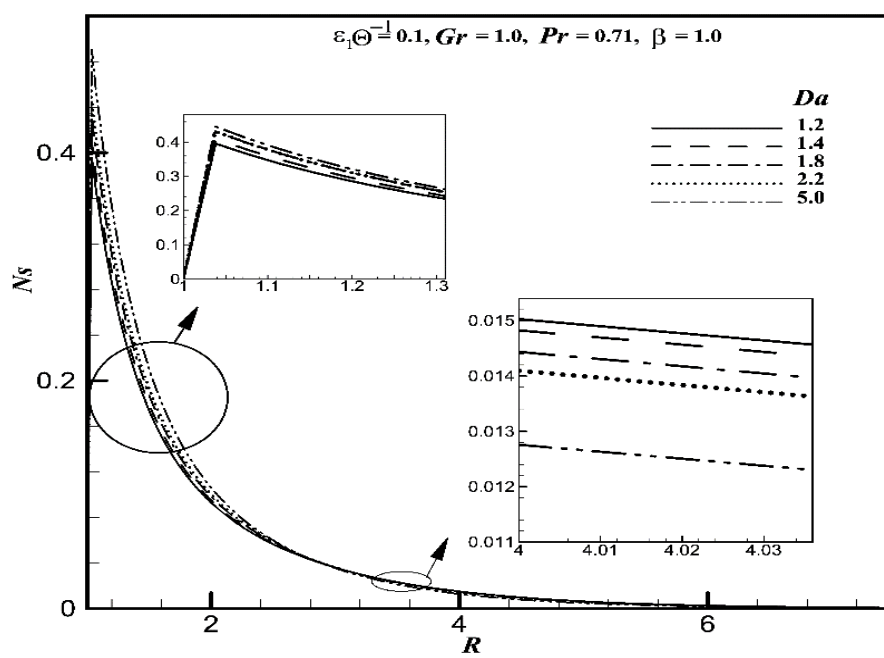
9. The transient entropy generation number (Ns) against time the point (1, for different values of (a) Da ; (c)



(10a)



(10b)



(10c)

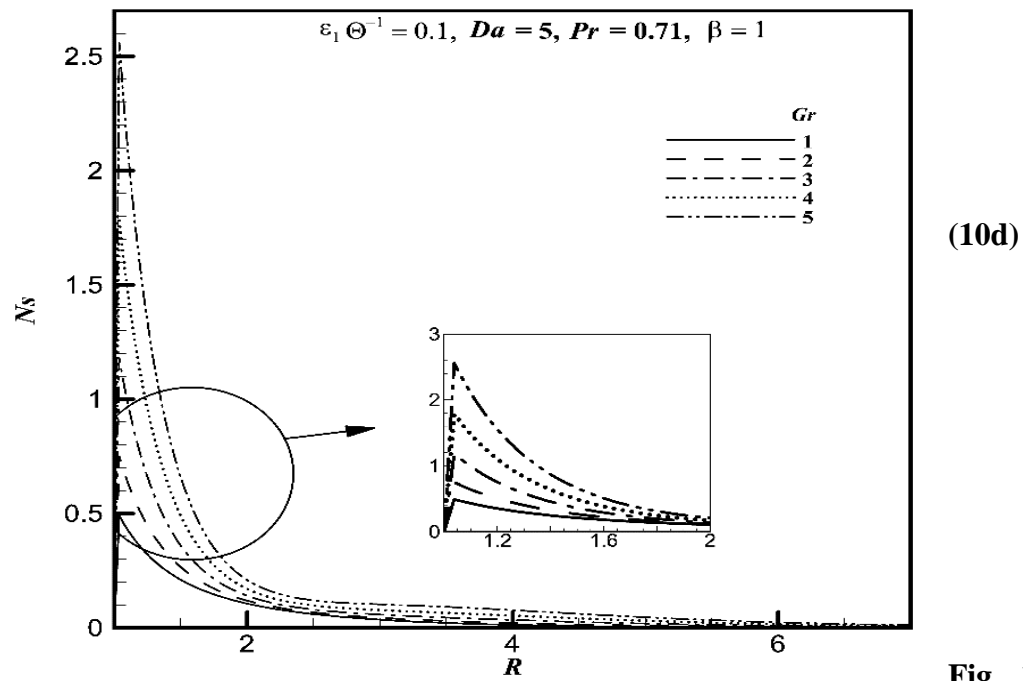
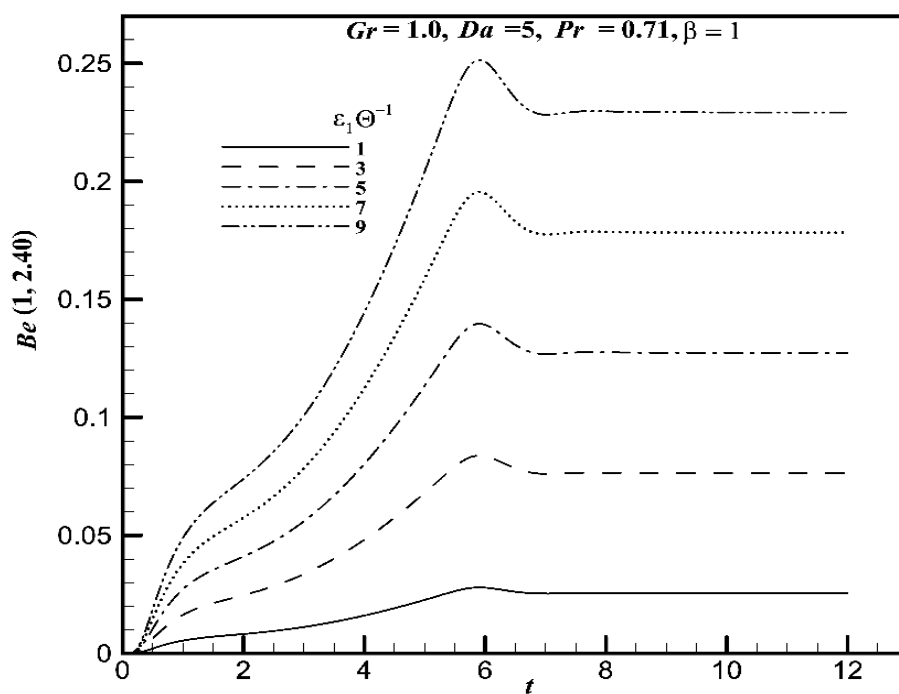
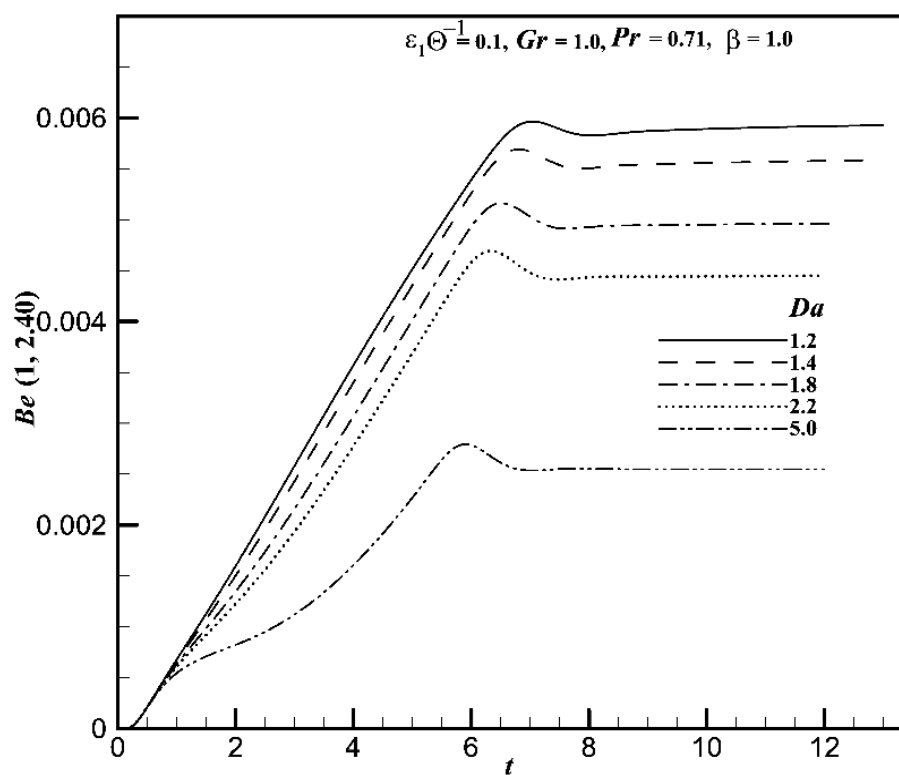


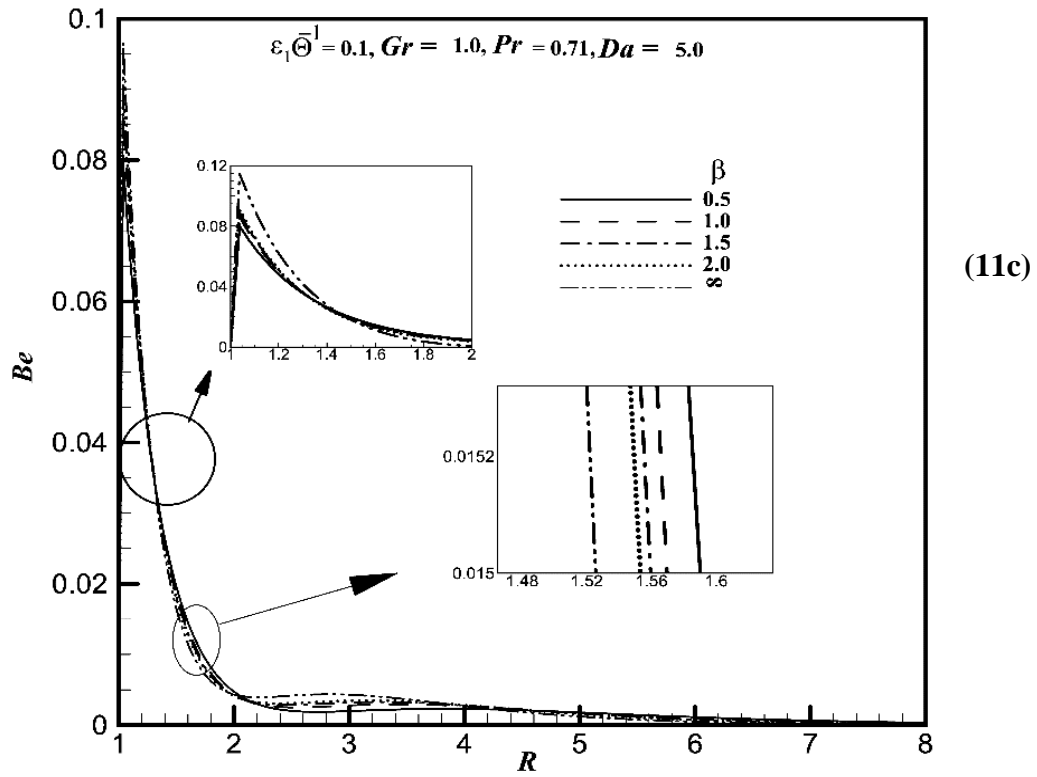
Fig. 10. The steady-state entropy generation number (N_s) against R at $X = 1.0$ for different values of (a) β ; (b) Da ; (c) $\varepsilon_1 \theta^{-1}$; & (d) Gr .



(11a)

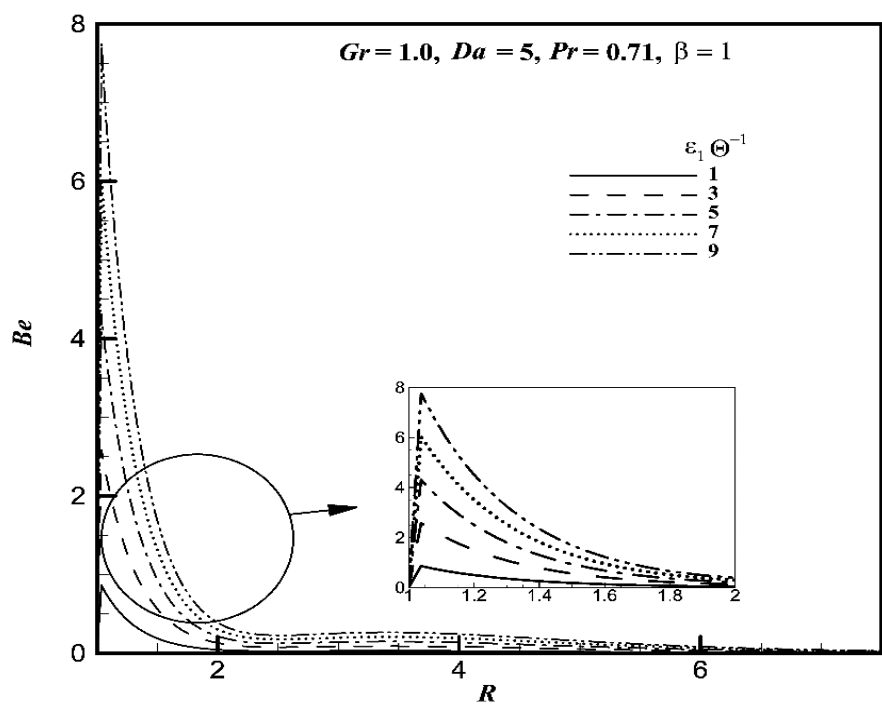


(11b)

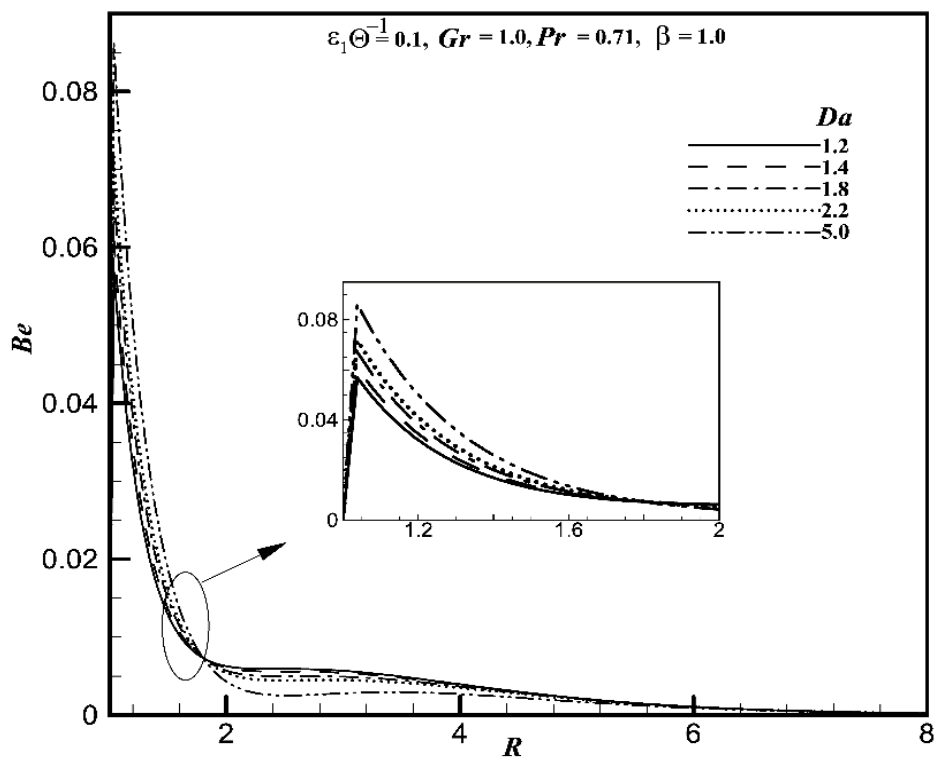


(11d)

Fig. 11. The transient Bejan number (Be) against time (t) at the location (1, 2.40) for different values of (a) β ; (b) Da ; (c) $\epsilon_1 \bar{\theta}^{-1}$; & (d) Gr .



(12a)



(12b)

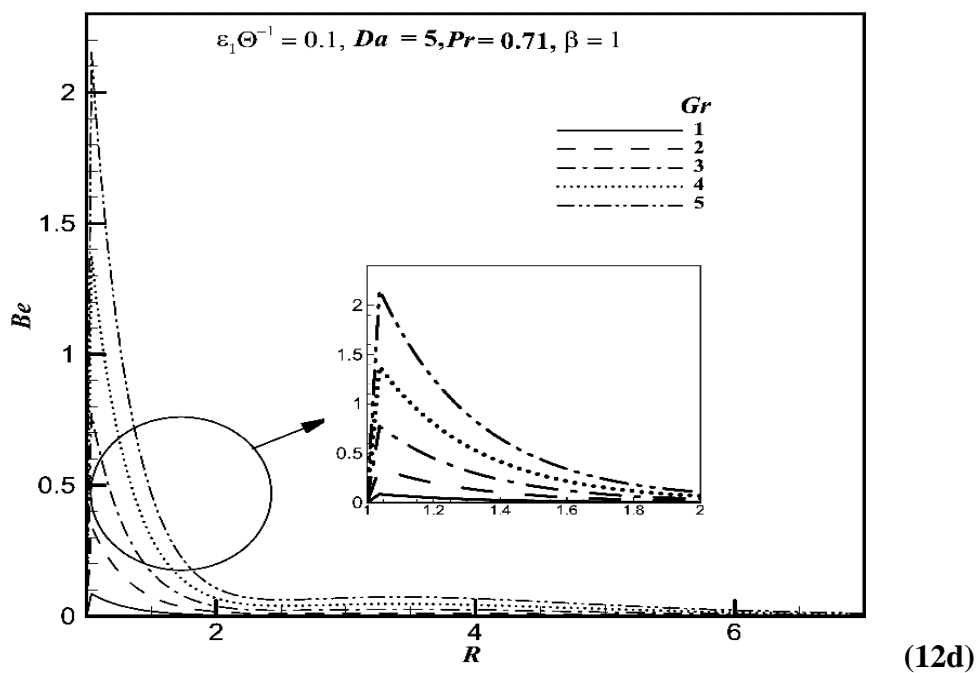
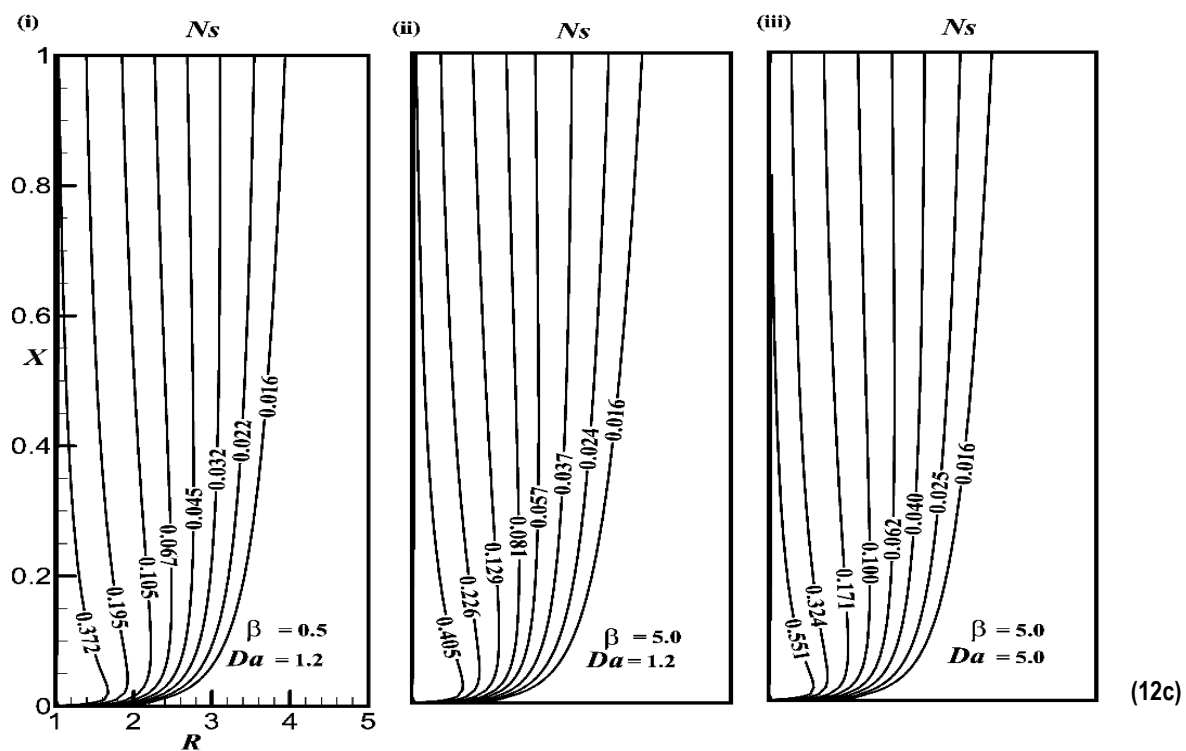
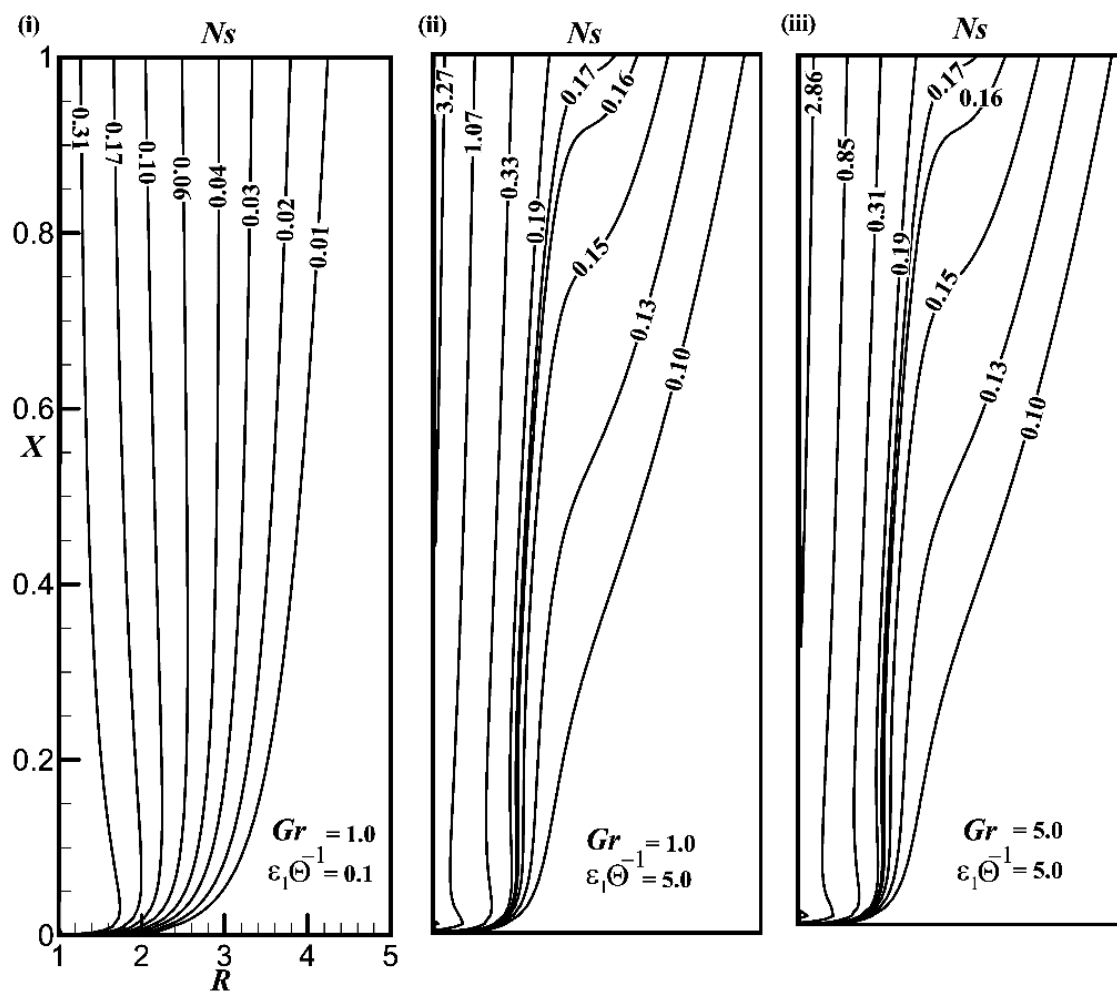
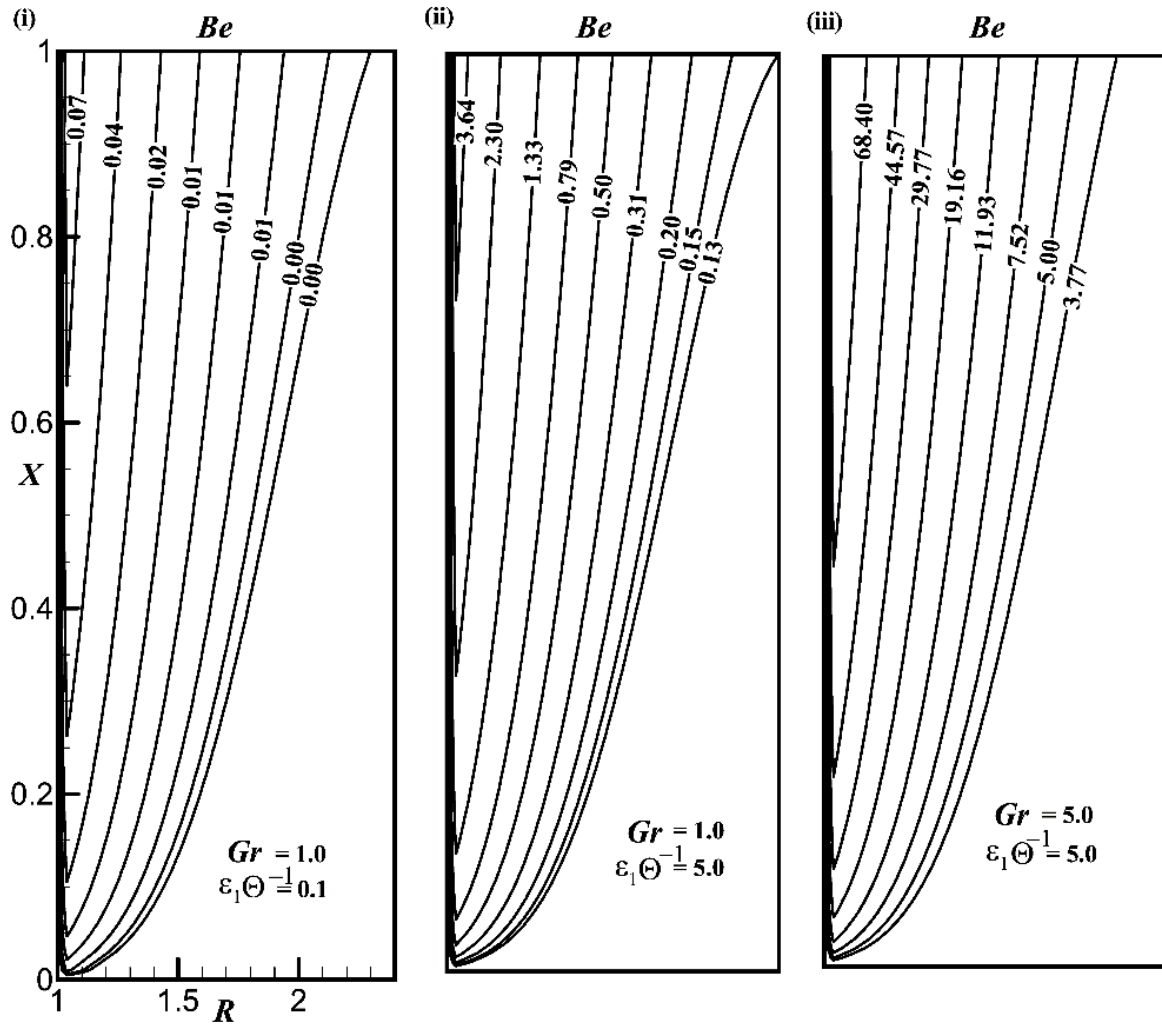


Fig. 12. The steady-state Bejan number (Be) against R at $X = 1.0$ for different values of (a) β ; (b) Da ; (c) $\epsilon_1 \theta^{-1}$; & (d) Gr .

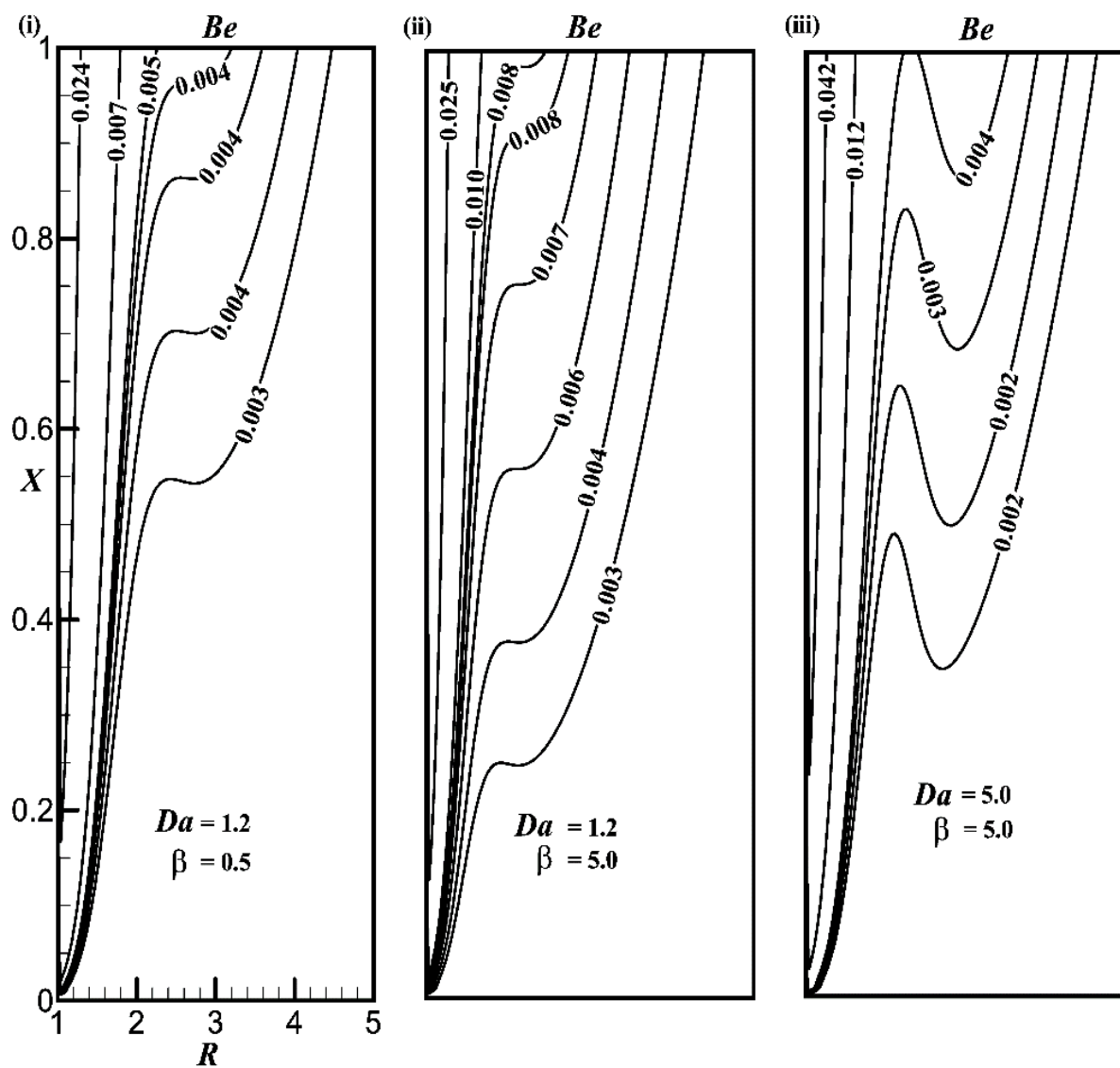


(13a)



(13b)

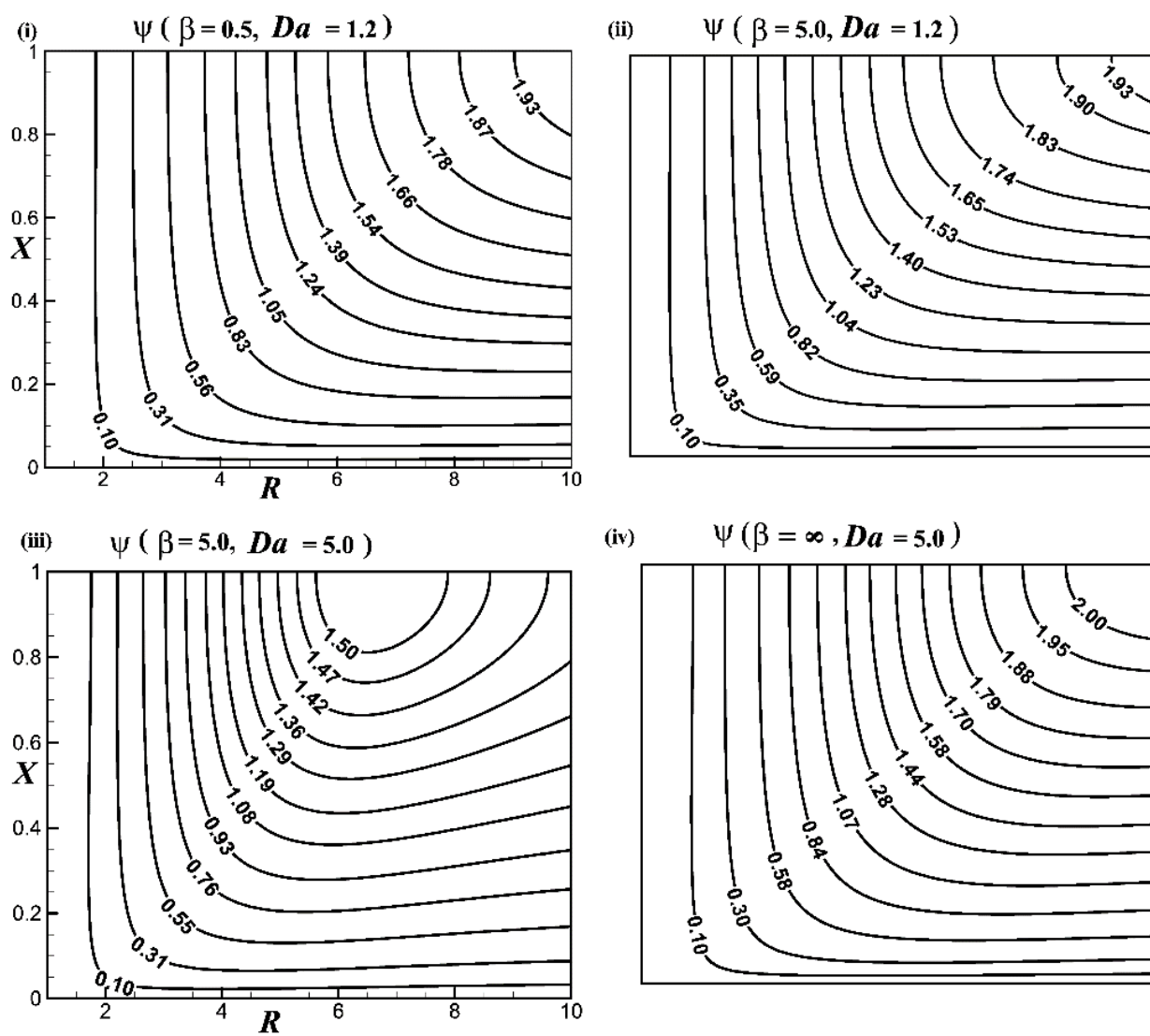
Fig. 13. Simulated steady-state entropy lines (N_s) in 2D coordinate system (X, R) for various values of (a) β and Da ; & (b) $\varepsilon_1 \Theta^{-1}$ and Gr .



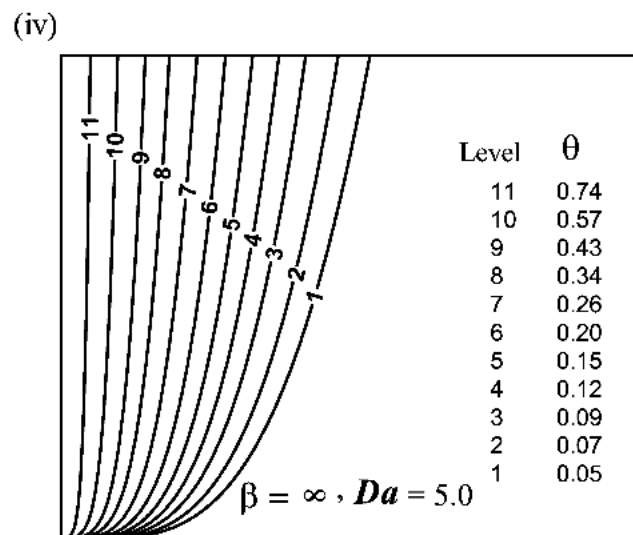
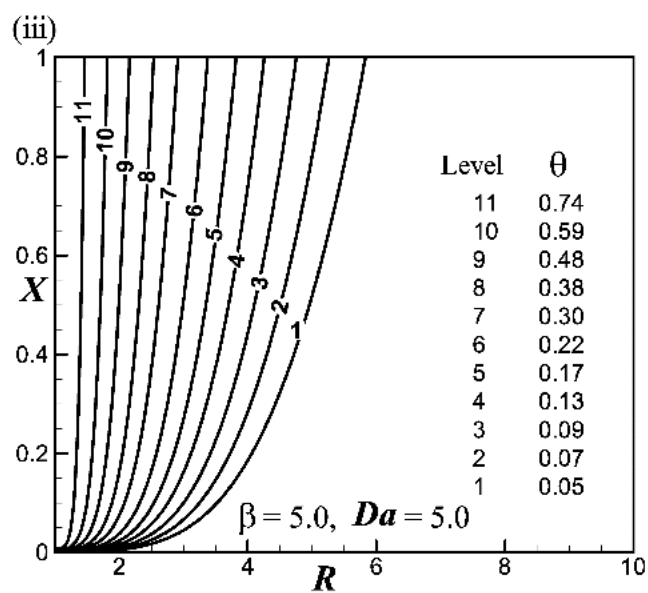
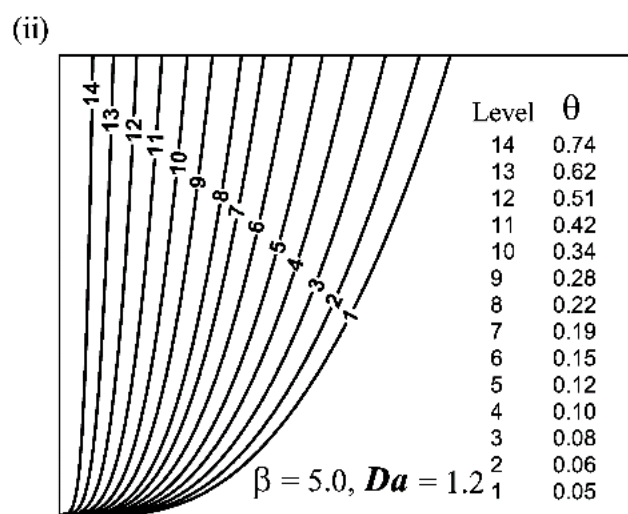
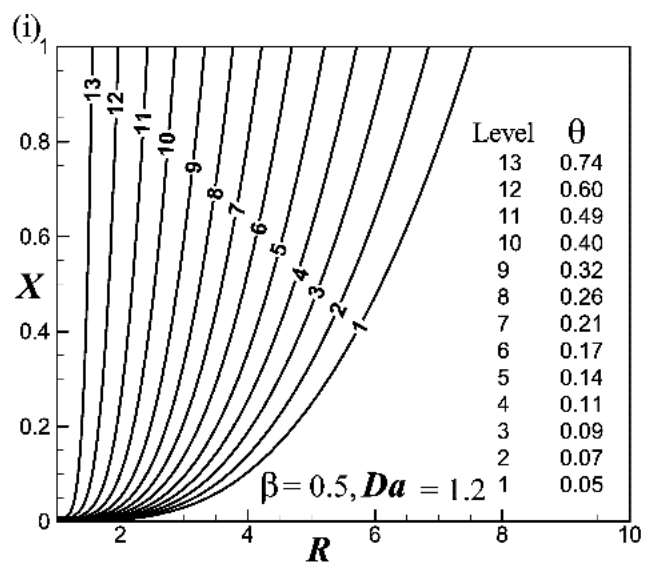
(14a)

(14b)

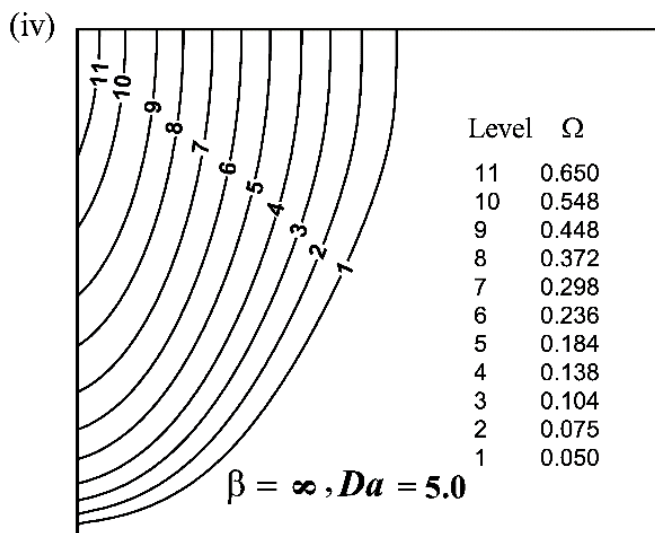
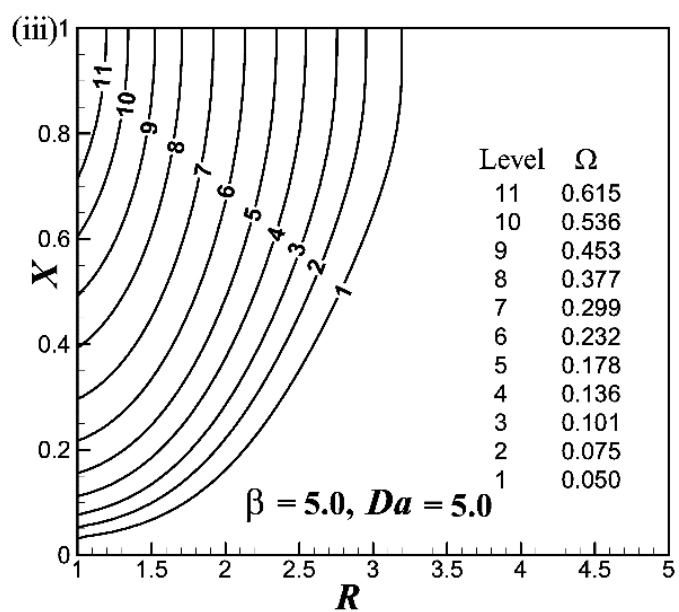
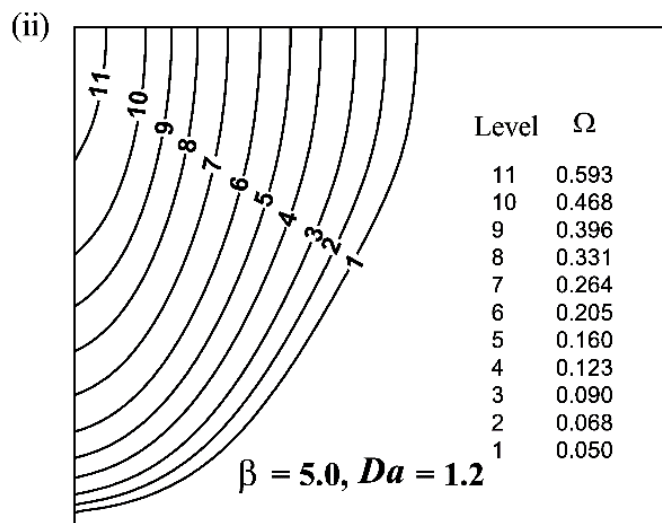
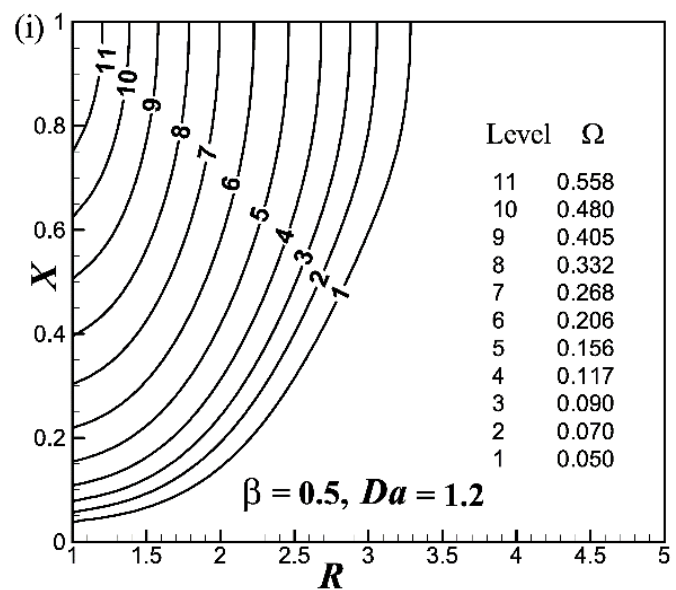
Fig. 14. Simulated steady-state Bejan lines (Be) in 2D coordinate system (X, R) for various values of (a) β and Da ; & (b) $\varepsilon_1\theta^{-1}$ and Gr .



(15a)



(15b)



(15c)

Fig. 15. Time-independent state (a) streamlines (ψ); (b) isotherms (θ); & (c) heatlines (Ω) in 2D coordinate system (X, R) for various values of β and Da with fixed value of $Pr = 0.71$.

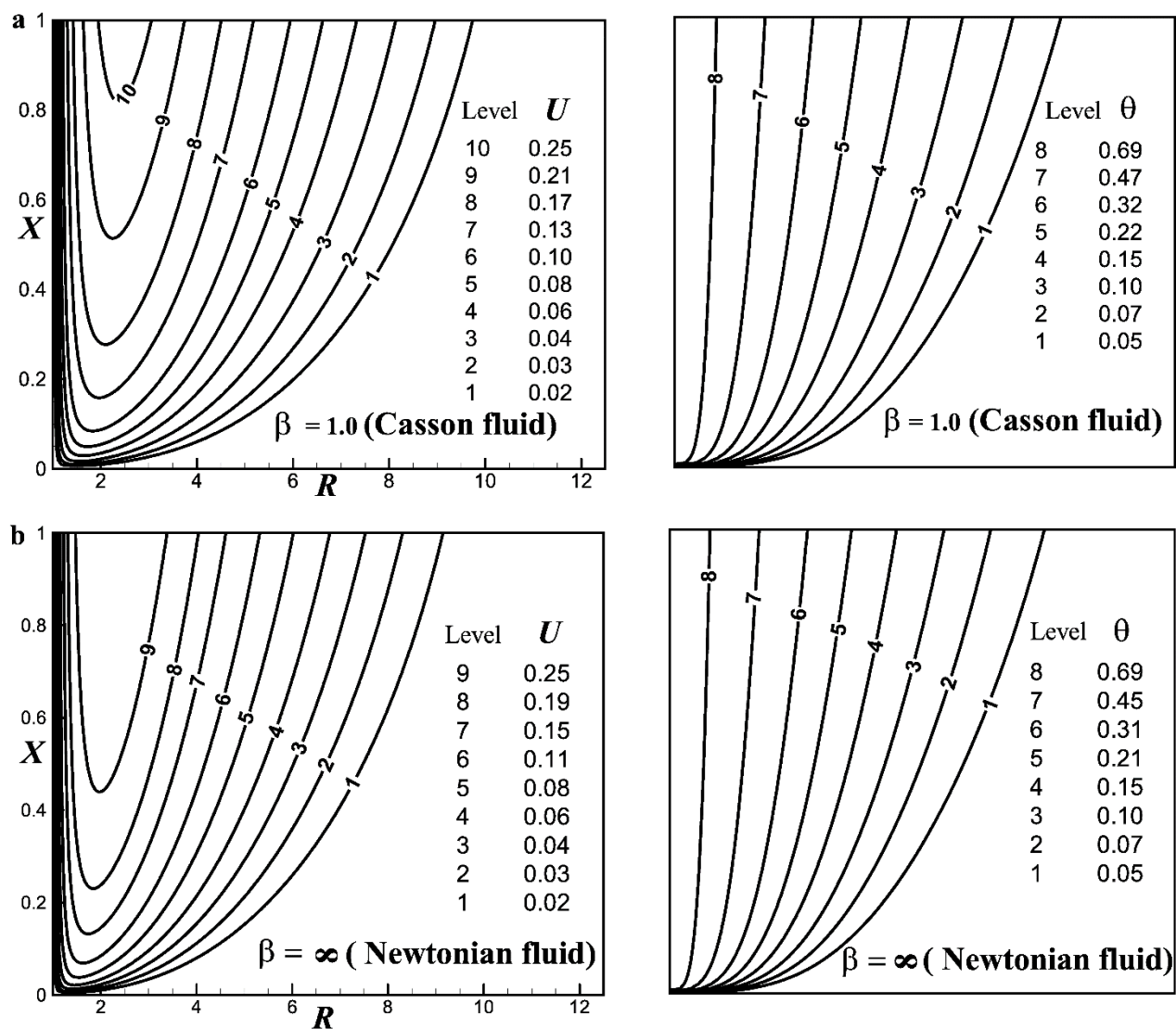


Fig. 16. Time-independent state contours of velocity (U) and temperature (θ) in 2D coordinate system (X, R) with fixed values of $Pr = 0.71$ and $Da = 1.2$ for **(a)** Casson fluid ($\beta = 1.0$); & **(b)** Newtonian fluid ($\beta = \infty$).